JM PAPERS

Turbulence ingestion noise generation in rotating blades

Henrique Raposo[1],† and Mahdi Azarpeyvand[1]

[1]Department of Aerospace Engineering, University of Bristol, Bristol BS8 1TR, UK

The interaction between ingested turbulence and rotating blades is a key source of broadband noise in engineering applications. In this paper, a far-field noise model accounting for source correlation across the span of the blade and between blades is developed and applied to the study of homogeneous isotropic turbulence ingestion by a model cooling fan, wind turbine and aircraft propeller. The widely used theory of Amiet is revisited and it is shown that previous works produce conflicting results when attempting to account for blade-to-blade correlation. Central to the model is the calculation of the time between blade chops of the same turbulent eddy as heard by the observer. In this paper it is shown that, when derived correctly, Amiet's theory accounts for correlated sources between blades and, thus, can predict haystacking tones. Comparisons with the new rotational formulation and with experimental data enable us to show that Amiet's theory can be used to accurately predict turbulence ingestion noise from open rotors. In particular, it is found that the infinite-span assumption in strip theory and the neglect of correlation effects across the span do not undermine the accuracy of this theory. This is of great importance because, unlike Amiet's theory, models which treat rotational effects and source correlation exactly are expensive to evaluate routinely at high frequencies due to the slow convergence of infinite series with Bessel functions.

Key words: aeroacoustics, homogeneous turbulence

1. Introduction

Noise generation in rotating blades is a problem of great interest in several engineering industries such as those of wind turbines, aeroengines and cooling fans. In the aeronautical sector, noise emission levels for certification are increasingly stringent and, as a result,

† Present address: Flight Physics Department, Vertical Aerospace Group Ltd., Bristol BS2 0UW, UK. Email address for correspondence: hctr.tome@gmail.com

large research programmes are devoted to developing new technologies to improve designs. Clean Sky 2, for example, aims to cut aircraft perceived noise levels by 20–30 % with respect to 2014 levels, on top of a 50 % reduction targeted by its predecessor as compared with 2000 levels (Brouckaert *et al.* 2018). The emergence of urban air mobility and the drive to electrify conventional aircraft are also creating new challenges in what concerns noise emissions. Distributed electric propulsion systems have enabled the exploration of a wider design space which has led to new research questions beyond those posed by traditional airframes and jet engines. In particular, many new aircraft concepts present architectures with multiple propellers. Examples include the Airbus Vahana, ZEROe and Lilium Jet.

Turbulence ingestion noise is the focus of this paper. This noise source is associated with stochastic unsteady pressure fluctuations on the blades caused by the interaction with upstream turbulence. It is broadband in nature but its spectrum often exhibits quasi-tonal peaks at multiples of the blade-passing frequency due to haystacking. The relative importance of this noise source compared with tonal noise or broadband self-noise is dependent on the particular rotor and operating conditions (Glegg & Devenport 2017). For example, turbulence ingestion noise is known to be dominant in static outdoor tests, while being comparatively subdued in forward flight at constant propeller speed and power (Hubbard 1991). It also becomes more prominent in rotors with reduced tip speeds where tonal noise loses its dominance over broadband noise sources. A competent discussion of these competing noise sources is found in § 16.1 of Glegg & Devenport (2017).

The research by Sharland (1964) was one of the earliest studies to recognise that turbulence in the approach stream to a rotor can increase noise levels significantly. Sevik (1974) measured the noise generated by a 10-bladed propeller ingesting grid turbulence. The accompanying theory, while in good agreement with measurements, did not consider the possibility of blade-to-blade loading coherence and, thus, haystacking peaks at harmonics of the blade-passing frequency were not predicted, in contrast to experimental observations. Haystacking was explained by Hanson (1974) who performed experiments in static aircraft engine fans. It was found that upstream atmospheric turbulence is stretched into thin elongated eddies by the contracting flow on approach to the fan. This highly anisotropic turbulence at the fan inlet is 'chopped several times as it passes through the rotor' (Hanson 1974). The partial blade-to-blade loading coherence leads to narrow-band noise around harmonics of the blade-passing frequency, also known as haystacking.

Hanson's theoretical formulation and other works preceding it (Lowson & Ollerhead 1969; Morfey & Tanna 1971) focused on the relation between the unsteady blade forces and noise, thus requiring experimental input. The first complete model of turbulence ingestion noise in rotating blades linking a free-stream turbulence input to noise was presented by Homicz & George (1974). The authors used a low-frequency compressible Sears aerofoil response function to calculate the unsteady lift generated by gust–aerofoil interaction, and proceeded to calculate the far-field pressure spectrum based on a spanwise and chordwise compact blade assumption which allows each blade to be reduced to a rotating dipole. These assumptions restrict the use of this theory to acoustic wavelengths several times longer than the aerofoil chord. Amiet (1977) and Paterson & Amiet (1979) overcame these limitations by recognising that the rotational blade motion can be assumed rectilinear on the time scales of noise generation provided that the acoustic frequency is much larger than the rotor velocity, i.e. $\omega \gg \Omega$. The noise radiated by rotating blades could thus be calculated on the basis of an earlier theory for stationary aerofoils in uniform flow (Amiet 1975), valid for both low and high frequencies, and including blade non-compactness effects. Sinayoko, Kingan & Agarwal (2013) noted that different formulations of Amiet's

theory for rotating blades existed in the literature and proceeded to identify the correct form. Karve, Angland & Nodé-Langlois (2018) extended Amiet's approach to account for installation effects, e.g. from a nearby wing surface, using the method of images and applied it to a boundary layer ingestion configuration.

Majumdar & Peake (1998) developed a theoretical model of unsteady turbulence distortion on approach to an open rotor with a large number of blades. This work built on Hanson's observation that the elongation of turbulent eddies is a key physical mechanism in turbulence ingestion noise. Extensive reviews of rapid distortion of turbulence into an open rotor can be found in Robison & Peake (2014) and Graham (2017). Majumdar & Peake (1998) used the distorted turbulence spectrum at the rotor face to calculate the unsteady blade loading with a two-dimensional response function for a linear cascade of flat plates (Smith 1972). This was combined with a Green's function approach to calculate the far-field noise. This method treats rotational effects in an exact manner and includes strip-to-strip correlation effects, while Amiet's approach (Amiet 1977) expresses noise as the sum of the individual, uncorrelated contributions of each strip. On the other hand, Amiet's approach accounts for three-dimensional gusts in each blade strip whereas the theory of Majumdar & Peake (1998) requires a two-dimensional approximation. Several aspects of the theories of Amiet (1977) and Majumdar & Peake (1998) can be modified or improved. In particular, the flat plate approximation oversimplifies the propeller geometry and neglects non-uniform mean flow effects. A detailed literature review of aerofoil leading edge noise in non-uniform flows can be found in the recent work of Zhong *et al.* (2020).

Glegg, Morton & Devenport (2012) proposed an alternative frequency-domain method to predict both near- and far-field noise from rotating blades with compact chords. The method is particularly useful in boundary layer ingestion configurations where the ingested turbulence is inhomogeneous and anisotropic. Glegg, Devenport & Alexander (2015) argued that frequency-domain approaches, such as those of Majumdar & Peake (1998) and Glegg *et al.* (2012), can be expensive to evaluate because the infinite series involving Bessel functions are slow to converge at high frequencies. Moreover, the authors stated that Amiet's approach 'assumes that the source at each blade section is uncorrelated across the span, and blade to blade, and so it does not predict the rotor tone noise or haystacking tones'. On this basis, the authors proceeded to develop a time-domain approach with a compact chord assumption based on the work of Casper & Farassat (2004). It was highlighted how direct measurements of two-point velocity correlations in the rotor plane can be used to estimate the upwash velocity cross-spectrum in the blade-fixed coordinate system. The purported advantages of this time-domain approach are that it is faster to evaluate than frequency-domain methods and also that it can be used in conjunction with direct flow measurements, avoiding the modelling of the turbulence spectra.

Sinayoko *et al.* (2013) compared Amiet's theory for trailing edge noise in rotating blades against a new formulation which models the rotational motion of the blades exactly. It was found that Amiet's theory remains valid even when the assumption that $\omega \gg \Omega$ is not formally respected. In addition, the authors identified the correct exponent of the Doppler factor which accounts for the relative motion between the source and the observer. This aspect of Amiet's theory is also relevant for turbulence ingestion noise. Comparisons between the two models were restricted to a single narrow strip of the blade and therefore the assumptions made by strip theory were not investigated.

In this paper we develop a turbulence ingestion noise model and compare it with Amiet's theory for three different rotor types: (i) a cooling fan, (ii) an open propeller and (iii) a wind turbine. This new model accounts for the rotational motion of the blades using

the same theoretical basis as Sinayoko *et al.* (2013). However, in contrast to their trailing edge noise theory, our model of turbulence ingestion noise accounts for source correlation effects across the blade span in a similar way to the model of Majumdar & Peake (1998). Amongst other reasons, our neglect of turbulence distortion by the steady non-uniform mean flow on approach to the rotor enables further analytical development than in the work of Majumdar & Peake (1998). We also re-derive Amiet's theory and we revisit an aspect of this theory which is particular to the problem of turbulence ingestion noise, i.e. blade-to-blade correlation. Amiet (1989) outlined an approach to include this effect into the calculations. Central to the model is the calculation of the time between blade chops of the same turbulent eddy as heard by the observer. Karve *et al.* (2018) used Amiet's model to show that theoretical predictions agree reasonably well with experimental results for noise generated due to turbulent boundary layer ingestion. However, Amiet (1989) and Karve *et al.* (2018) disagree on the calculation of the time between blade chops. In this paper, we derive this result in a simple and clear way, and identify the correct form by comparing far-field noise predictions against the rotational model of turbulence ingestion noise. It is shown that, when derived correctly, Amiet's theory can account for correlated sources between blades and, thus, it can predict haystacking tones. This is confirmed through comparisons with experimental data.

Another aspect of the rotational model that differs from Amiet's theory is that noise prediction from the whole rotor does not require employing a stripping method. Amiet's theory can be formulated assuming that each strip has finite span, but this is known to lead to far-field noise predictions that are dependent on the number of strips, particularly at low frequencies (Christophe, Anthoine & Moreau 2009). Alternatively, an infinite-span assumption can be introduced to remove the problem of choosing an arbitrary number of strips. This is often the preferred approach, even though our current understanding of the effect of this assumption is limited to stationary wings (Christophe *et al.* 2009; Christophe 2011). Comparisons between Amiet's theory and the new rotational formulation in model rotors enable us to study the validity of the infinite-span assumption as well as the effect of neglecting correlation effects across the span. Overall, this paper aims to clarify whether Amiet's theory can be used to accurately predict turbulence ingestion noise from open rotors. This is of great importance because models such as those of Majumdar & Peake (1998) and Glegg *et al.* (2012, 2015) are comparatively expensive to evaluate routinely.

The remainder of this paper is structured as follows. In § 2, we derive the turbulence ingestion noise model which accounts for the rotational motion of the blades and for source correlations across the blade span and between blades. It is shown that in the low advance ratio limit considerable simplifications can be made such that only the streamwise turbulent velocity fluctuations are required to predict turbulence ingestion noise. In § 3, we re-derive Amiet's theory, discussing in detail the calculation of the time between blade chops as heard by the observer. In § 4, we proceed to compare the two turbulence ingestion noise models for a model cooling fan, wind turbine and aircraft propeller. We examine the turbulent upwash velocity cross-spectrum in § 4.3 and the far-field noise in § 4.4. Lastly, both noise models are validated through comparisons with experimental data in § 4.5.

2. Turbulence ingestion noise model for rotating blades

2.1. *Pressure field in the frequency domain*

Consider the problem of leading-edge noise radiation from a stationary rotor ingesting turbulence convected by a uniform flow with axial Mach number M_z. The observer is stationary with respect to the rotor hub. Further consider a fixed Cartesian coordinate
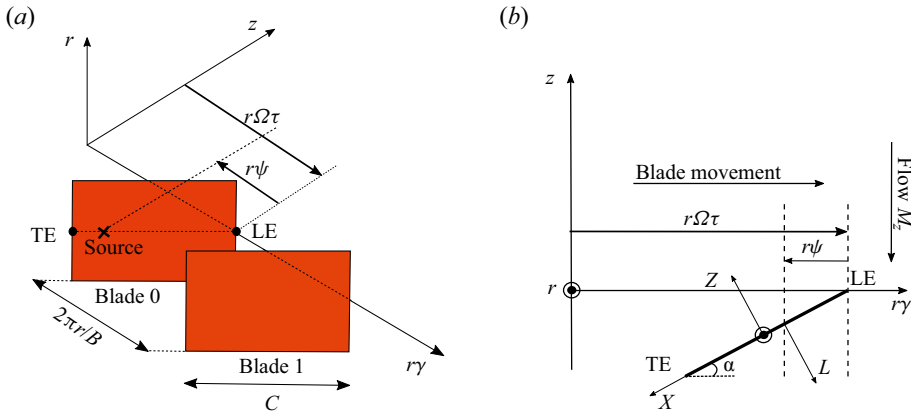
Figure 1. Blade geometry and source position in cylindrical coordinate system $(r, \gamma = \Omega\tau + \psi + 2\pi m/B, z)$. Figure adapted from Sinayoko *et al.* (2013). (*a*) Three-dimensional view of the blade geometry showing the cross-blade spacing in the unwrapped blade path. (*b*) Zeroth blade geometry and blade-fixed coordinate system (X, Y, Z) in the plane (z, γ).

system positioned at the centre of the hub. The z-axis is aligned with the uniform flow and points upstream. The x-axis points vertically upwards in the rotor plane and the y-axis is such that the coordinate system is right-handed. Figure 1 shows the geometry of the blades in the source cylindrical coordinate system (r, γ, z), where the azimuthal direction γ has been unwrapped. Both lean and sweep are neglected. The cross-sections of the blades are assumed to be flat plates of chord C. The pitch change axis is located at the leading edge and the pitch angle, α, is assumed to vary in the radial direction such that blade cross-sections are at zero angle of attack relative to the incoming flow

$$\alpha = \arctan\left(\frac{U_z}{\Omega r}\right), \tag{2.1}$$

where U_z is the axial flow velocity and Ω is the rotor angular velocity. The blade-fixed coordinate system (X, Y, Z) is centred mid-chord with the X-axis in the downstream direction and the Z-axis in the wall-normal direction. Two consecutive blades are separated by a distance of $2\pi r/B$ in the unwrapped azimuthal direction, where B is the number of blades. The azimuthal angle of a source in the mth blade planform, where $m \in [0, B-1]$, is given by $\gamma = \Omega\tau - \psi + \phi_m$, where τ is the emission time and $\phi_m = 2\pi m/B$. For clarity, let us define the Fourier transform pair $(f, \tilde{f})$ used throughout this paper:

$$\tilde{f}(\omega) = \frac{1}{2\pi} \int_{-\infty}^{+\infty} f(t) e^{-i\omega t}\, dt, \quad f(t) = \int_{-\infty}^{+\infty} \tilde{f}(\omega) e^{i\omega t}\, d\omega. \tag{2.2a,b}$$

We note that the notation of this section has largely been adopted from Sinayoko *et al.* (2013). The pressure field generated by the mth blade due to interaction with the incoming turbulent flow is given by (Sinayoko *et al.* 2013)

$$\tilde{p}^{(m)}(x_o, \omega) = 2\pi i \tilde{g} \sum_{n=-\infty}^{+\infty} \exp(-in(\gamma_0 - \pi/2)) \int_{\Sigma} k_L J_n(k_r r) \tilde{L}^{(m)}(x, \omega - n\Omega)$$

$$\times \exp(-i[k_C(X + C/2) - n\phi_m])\, d\Sigma, \tag{2.3}$$

where

$$\tilde{g}(k, R_e, \theta_e) = \frac{e^{-ikR_e}}{8\pi^2 R_e(1 - M_z \cos\theta_e)}, \tag{2.4}$$

and with the integration performed over the blade planform Σ. We use $\tilde{L}$ to denote the unsteady lift force per unit area and J_n to represent the nth Bessel function of the first kind. The vectors x and x_o denote, respectively, the current source position and the observer position in the hub-fixed Cartesian coordinate system. The vector X denotes the current source position in the blade-fixed Cartesian coordinate system. We have also introduced $(R_e, \theta_e, \gamma_0)$ to denote the observer position in spherical emission coordinates (Sinayoko *et al.* 2013), given by

$$x_o = R_e \sin\theta_e \cos\gamma_0, \tag{2.5a}$$

$$y_o = R_e \sin\theta_e \sin\gamma_0, \tag{2.5b}$$

$$z_o = R_e (\cos\theta_e - M_z). \tag{2.5c}$$

The acoustic wave frequency and wavenumber are given by ω and $k = \omega/c_0$, respectively, where c_0 is the speed of sound. The modal wavenumbers in the blade-fixed coordinate system are given by

$$k_L = k_z \cos\alpha - (n/r)\sin\alpha, \quad k_C = k_z \sin\alpha + (n/r)\cos\alpha, \tag{2.6a,b}$$

where

$$k_z = k\cos\theta_e/(1 - M_z \cos\theta_e), \quad k_r = k\sin\theta_e/(1 - M_z \cos\theta_e). \tag{2.7a,b}$$

2.2. Aeroacoustic transfer function

The far-field pressure expression presented in § 2.1 remains a function of the lift forces acting on the blade. We proceed to calculate the unsteady lift generated by the blades as a consequence of turbulence ingestion by the rotor. Let us consider a two-dimensional turbulence gust impinging on a blade cross-section. Its upwash velocity is given by

$$w_g(X, t) = \tilde{w}_g(k_X)\exp(ik_X(U_rt - X)), \tag{2.8}$$

where $U_r = \sqrt{U_z^2 + U_\gamma^2}$ is the blade relative velocity, and $U_\gamma = \Omega r$ is the tangential velocity. The streamwise wavenumber is given by $k_X = \omega/U_r$. Taylor's frozen turbulence hypothesis has been adopted here. We can introduce the aerofoil response function, g, by writing the unsteady lift produced by the aerofoil interaction with a single sinusoidal gust as (Amiet 1975)

$$L(X, t) = 2\pi\rho U_r g(X, k_X)\tilde{w}_g(k_X)e^{i\omega t}, \tag{2.9}$$

where ρ denotes the far-field uniform flow density. Note that the oscillatory behaviour in the X direction has been absorbed into the aerofoil response function (g). The equivalent frequency-domain result is obtained by integrating the contributions of all wavenumbers and taking the Fourier transform. Its final form is (Amiet 1975)

$$\tilde{L}(X, \omega) = 2\pi\rho U_r g(X, k_X)\tilde{w}_g(\omega), \tag{2.10}$$

where we have used $\tilde{w}_g(k_X) = U_r\tilde{w}_g(\omega)$. A detailed derivation of $g(X, k_X)$ in the high-frequency regime, following Amiet's theory (Amiet 1976a), can be found in

980 A53-6

Appendix C.1 of Christophe (2011). Substituting (2.10) in the pressure field generated by the mth blade (2.3) yields

$$
\tilde{p}^{(m)}(\boldsymbol{x}_o, \omega) = \frac{\mathrm{i}\rho \exp(-\mathrm{i}kR_e)}{2R_e(1 - M_z \cos\theta_e)} \sum_{n=-\infty}^{+\infty} \int_{r_{hub}}^{r_{tip}} k_L \mathrm{J}_n(k_r r) U_r \tilde{w}_g^{(m)}(r, \omega - n\Omega)
$$

$$
\times \exp(\mathrm{i}n(-\gamma_0 + \pi/2 + \phi_m)) \exp(-\mathrm{i}k_C C/2) \int_{-C/2}^{C/2} g(X, \mathrm{K}_X)
$$

$$
\times \exp(-\mathrm{i}k_C X) \,\mathrm{d}X \,\mathrm{d}r, \tag{2.11}
$$

where $\mathrm{K}_X = (\omega - n\Omega)/U_r$. The aeroacoustic transfer function is defined as

$$
\mathcal{L}(k_X, k_C) = \frac{2}{C} \int_{-C/2}^{C/2} g(X, k_X) \exp(-\mathrm{i}k_C X) \,\mathrm{d}X. \tag{2.12}
$$

The definition of the aeroacoustic transfer function (2.12) can finally be introduced in (2.11), yielding

$$
\tilde{p}(\boldsymbol{x}_o, \omega) = \frac{\mathrm{i}C\rho \exp(-\mathrm{i}kR_e)}{4R_e(1 - M_z \cos\theta_e)} \sum_{m=0}^{B-1} \sum_{n=-\infty}^{+\infty} \int_{r_{hub}}^{r_{tip}} k_L \mathrm{J}_n(k_r r) U_r \tilde{w}_g^{(m)}(r, \omega - n\Omega)
$$

$$
\times \exp(\mathrm{i}n(-\gamma_0 + \pi/2 + \phi_m) - \mathrm{i}k_C C/2)\mathcal{L}(\mathrm{K}_X, k_C) \,\mathrm{d}r, \tag{2.13}
$$

where we have summed the contributions of each blade to obtain the total far-field pressure $\tilde{p}(\boldsymbol{x}_o, \omega)$.

The aeroacoustic transfer function defined in (2.12) is a more general transfer function than typically found in the literature because k_C has not been substituted by a specific value. The first-order term in Amiet's high-frequency successive approximation method is given by (Amiet 1976a)

$$
\mathcal{L}_1(k_X, k_C) = -\frac{\mathrm{i}e^{\mathrm{i}\bar{k}_C}}{\pi\sqrt{\bar{k}_X + \beta_r^2 \kappa}\sqrt{\kappa - \bar{k}_X' M_r^2 + \bar{k}_C}} \mathrm{erf}\left[(1 + \mathrm{i})\sqrt{\kappa - \bar{k}_X' M_r^2 + \bar{k}_C}\right], \tag{2.14}
$$

where $k_X' = k_X/\beta_r^2$, $\beta_r = \sqrt{1 - M_r^2}$, $\kappa = \bar{k}_X' M_r$, $M_r = U_r/c_0$ and the overbar denotes quantities made non-dimensional with the length scale $C/2$. The error function of complex argument, $\mathrm{erf}(z)$, is defined as

$$
\mathrm{erf}(z) = \frac{2}{\sqrt{\pi}} \int_0^z \mathrm{e}^{-t^2} \,\mathrm{d}t. \tag{2.15}
$$

The back-scattering correction is given by

$$
\mathcal{L}_2(k_X, k_C) = \frac{\exp(\mathrm{i}(\pi/4 + \bar{k}_C))}{\theta_1 \pi \sqrt{2\pi\left(\bar{k}_X + \beta_r^2 \kappa\right)}} \Bigg[(1 - \exp(-2\mathrm{i}\theta_1)) + (1 + \mathrm{i})
$$

$$
\times \left[-E^*(4\kappa) + \sqrt{\frac{2\kappa}{2\kappa - \theta_1}} \exp(-2\mathrm{i}\theta_1) E^*\left(2(2\kappa - \theta_1)\right) \right] \Bigg], \tag{2.16}
$$

where $\theta_1 = \kappa - \bar{k}'_X M_r^2 + \bar{k}_C$, and the Fresnel integral is defined as

$$E^*(z) = \int_0^z \frac{e^{-it}}{\sqrt{2\pi t}}\, dt. \tag{2.17}$$

The aeroacoustic transfer function is thus given by $\mathcal{L} = \mathcal{L}_1 + \mathcal{L}_2$ or $\mathcal{L} = \mathcal{L}_1$, with and without trailing edge back-scattering effects, respectively.

For frequencies where the blade chord is compact we require another solution that is valid in the low-frequency regime, i.e. for $\omega C/2c_0(1 - M_r^2) < \pi/4$ (Amiet 1975). The pressure jump in this regime was studied by Amiet (1974) and the associated normalised aerofoil response function is given by (Amiet 1989)

$$g(\bar{X}, k_X) = \frac{1}{\beta_r \pi} \sqrt{\frac{1 - \bar{X}}{1 + \bar{X}}} S(\bar{k}'_x) \exp(i\bar{k}'_X(M_r^2 \bar{X} + f(M_r))), \tag{2.18}$$

where $f(M_r) = (1 - \beta_r) \ln(M_r) + \beta_r \ln(1 + \beta_r) - \ln(2)$, and $S(\bar{k}'_X)$ is the Sears function given by

$$S(\bar{k}'_X) = \frac{2}{\pi \bar{k}'_X \left(H_0^{(1)}(\bar{k}'_X) + iH_1^{(1)}(\bar{k}'_X) \right)}, \tag{2.19}$$

where $H_n^{(1)}$ is the Hankel function of order n of the first kind. Note that the Sears response function in (2.18) includes a compressibility correction. The interested reader is referred to Amiet (1974, 1993) for details. The aeroacoustic transfer function follows immediately

$$\mathcal{L}(k_X, k_C) = \frac{1}{\beta_r} S(\bar{k}'_X) \exp(i\bar{k}'_X f(M_r)) \left[J_0(\bar{k}'_x M_r^2 - \bar{k}_C) - iJ_1(\bar{k}'_X M_r^2 - \bar{k}_C) \right]. \tag{2.20}$$

2.3. *Far-field noise spectrum*

The pressure field generated by the propeller was linked to the incoming turbulence in §2.2 through an aeroacoustic transfer function for both low- and high-frequency gusts. We proceed to calculate the power spectral density by adopting the following definition

$$S_{pp}(\boldsymbol{x}_o, \omega) = \frac{\pi}{T} E\left[\tilde{p}(\boldsymbol{x}_o, \omega) \tilde{p}^*(\boldsymbol{x}_o, \omega) \right], \tag{2.21}$$

where $E[\ldots]$ denotes the expected value. Using (2.13) in this definition yields

$$\begin{aligned}
S_{pp}(\boldsymbol{x}_o, \omega) = {} & \frac{C^2 \rho^2}{16 R_e^2 (1 - M_z \cos \theta_e)^2} \sum_{m=0}^{B-1} \sum_{k=0}^{B-1} \sum_{n=-\infty}^{+\infty} \int_{r_{hub}}^{r_{tip}} \int_{r_{hub}}^{r_{tip}} k_L k'_L J_n(k_r r) J'_n(k'_r r') U_r U'_r \\
& \times S_{ww}^{(m,k)}(r, r', \omega - n\Omega) \\
& \times \exp\left(i\frac{2\pi n}{B}(m - k) - i(k_C - k'_C)C/2 \right) \mathcal{L}(K_X, k_C) \mathcal{L}^*(K'_X, k'_C)\, dr\, dr',
\end{aligned} \tag{2.22}$$

where

$$S_{ww}^{(m,k)}(r, r', \omega) = \frac{\pi}{T} E\left[\tilde{w}_g^{(m)}(r, \omega) \tilde{w}_g^{(k)*}(r', \omega) \right]. \tag{2.23}$$

The problem is thus reduced to calculating the blade-normal unsteady velocity cross-spectrum, $S_{ww}^{(m,k)}$. Following Glegg *et al.* (2012), the Fourier transform of the gust

velocity component normal to the blade is given by

$$\tilde{w}_g^{(m)}(r, \omega) = \frac{1}{2\pi} \int_{-T}^{T} n_i^{(m)}(r, \tau) v_i(x_{LE}^{(m)}(\tau), \tau) e^{-i\omega\tau} \, d\tau, \qquad (2.24)$$

where $v(x_{LE}^{(m)}(\tau), \tau)$ is the gust velocity vector in the hub-fixed coordinate system, which is a function of the mth blade's leading-edge position. The gust velocity is projected onto the blade-normal direction by taking the inner product with the unit normal vector. These are given by

$$x_{LE}^{(m)}(\tau) = \left[r \cos\gamma_{LE}, r \sin\gamma_{LE}, 0 \right]^{\mathrm{T}}, \qquad (2.25a)$$

$$n^{(m)}(r, \tau) = \left[-\sin\alpha \sin\gamma_{LE}, \sin\alpha \cos\gamma_{LE}, -\cos\alpha \right]^{\mathrm{T}}, \qquad (2.25b)$$

where $\gamma_{LE} = \Omega\tau + \phi_m$. Substituting (2.24) in (2.23) and defining the cross-correlation as $R_{ij}(x_{LE}^{(m)}, x_{LE}^{(k)}, \tau - \tau') = E[v_i v_j^*]$ yields

$$S_{ww}^{(m,k)}(r, r', \omega) = \frac{1}{4\pi T} \int_{-T}^{T} \int_{-T}^{T} n_i^{(m)}(r, \tau) n_j^{(k)}(r', \tau') R_{ij}(x_{LE}^{(m)}, x_{LE}^{(k)}, \tau - \tau')$$

$$\times \exp(i\omega(\tau' - \tau)) \, d\tau \, d\tau'. \qquad (2.26)$$

This expression can be used to calculate the upwash velocity cross-spectrum from the knowledge of the two-point velocity correlation in the plane of the rotor. This has the advantage of accounting for the distortion of turbulence on approach to the rotor, bypassing the modelling of this phenomena. It is particularly advantageous in cases where no wavenumber spectrum is readily available or when one has access to direct measurements of the velocity cross-correlation, see Glegg *et al.* (2015) as an example.

2.4. *Turbulent upwash velocity cross-spectrum*

In § 2.3, we derived an expression for the noise power spectral density which requires knowledge of the turbulent upwash velocity cross-spectrum in the blade-fixed coordinate system as an input. The upwash velocity cross-spectrum can be calculated directly with (2.26) from time-domain measurements of the turbulence velocity in the rotor plane, for example. However, in general it is more useful to express the upwash velocity cross-spectrum as a function of the impinging turbulent velocity spectrum in the hub-fixed coordinate system. Following Glegg *et al.* (2012), let us introduce the correlation–spectrum pair of a homogeneous turbulence field as

$$R_{ij}(x_{LE}^{(m)}, x_{LE}^{(k)}, \tau - \tau') = \int_{-\infty}^{+\infty} \Phi_{ij}(k) \exp(ik \cdot (x_{LE}^{(m)} - x_{LE}^{(k)}) + iU_z k_z(\tau - \tau')) \, dk, \quad (2.27)$$

where $k = [k_x, k_y, k_z]^{\mathrm{T}}$ is the wavenumber vector, and $\Phi_{ij}(k)$ is the turbulent velocity spectrum. Substituting this in (2.26), we obtain

$$S_{ww}^{(m,k)}(r, r', \omega) = \frac{1}{4\pi T} \int_{-\infty}^{+\infty} \Phi_{ij}(k) \int_{-T}^{T} \int_{-T}^{T} n_i^{(m)}(r, \tau) n_j^{(k)}(r', \tau')$$

$$\times \exp(i\omega(\tau' - \tau) + ik \cdot (x_{LE}^{(m)}(\tau) - x_{LE}^{(k)}(\tau')) + iU_z k_z(\tau - \tau')) \, d\tau \, d\tau' \, dk. \quad (2.28)$$

We introduce the Jacobi–Anger expansion of $\exp(\mathrm{i}\boldsymbol{k} \cdot \boldsymbol{x}_{LE}^{(m)}(\tau))$, to obtain

$$\exp(\mathrm{i}\boldsymbol{k} \cdot \boldsymbol{x}_{LE}^{(m)}(\tau)) = \exp(\mathrm{i}k_R r \cos(\Omega\tau + \phi_m - k_\gamma))$$

$$= \sum_{p=-\infty}^{+\infty} \mathrm{i}^p \mathrm{J}_p(k_R r) \exp(\mathrm{i}p(\Omega\tau + \phi_m - k_\gamma)), \qquad (2.29)$$

where $k_R^2 = k_x^2 + k_y^2$ and $k_\gamma = \arctan(k_y/k_x)$. The unit normal vector can be rewritten in terms of complex exponentials as

$$\boldsymbol{n}^{(m)}(r, \tau) = \left[-\sin\alpha \frac{\mathrm{e}^{\mathrm{i}(\Omega\tau+\phi_m)} - \mathrm{e}^{-\mathrm{i}(\Omega\tau+\phi_m)}}{2\mathrm{i}}, \sin\alpha \frac{\mathrm{e}^{\mathrm{i}(\Omega\tau+\phi_m)} + \mathrm{e}^{-\mathrm{i}(\Omega\tau+\phi_m)}}{2}, -\cos\alpha \right]^{\mathrm{T}}.$$
$$(2.30)$$

Using the expansion introduced in (2.29) for the mth and kth blades, and (2.30) in (2.28), we obtain the full cross-spectrum of the blade-normal gust velocity component; see Appendix A. Those expressions can be considerably simplified if we assume that the blades are untwisted, i.e. that the blade pitch angle is small $\alpha \ll 1$, leading to $\sin\alpha \approx 0$ and $\cos\alpha \approx 1$. This assumption is not uniformly valid along the blade radial direction. However, it can be argued that because turbulence ingestion noise scales with the fourth power of the blade relative velocity (Glegg & Devenport 2017), most of the far-field noise originates in the vicinity of the blade tip. In this region, assuming that the blades operate at low angles of attack, the pitch angle should be small due to the large ratio between the propeller azimuthal velocity and the uniform flow velocity. In this paper, we have made the simplifying assumption that the blades operate at zero angle of attack, and therefore the pitch angle is given by (2.1). At the blade tip, i.e. for $r = r_{tip}$, (2.1) can be written in terms of the advance ratio, $J = U_z\pi/\Omega r_{tip}$, as $\alpha_{tip} = \arctan(J/\pi)$. The blade tip pitch angle is thus smallest when the rotor is operating at lower advance ratios. Under this assumption, together with the argument that the majority of far-field noise originates in the blade tip region, the untwisted blade approximation should be valid. This is investigated in § 4 for a model cooling fan, an open propeller and a wind turbine. Introducing the approximations $\sin\alpha \approx 0$ and $\cos\alpha \approx 1$ in (A2) and substituting the result in (A1) yields

$$S_{ww}^{(m,k)}(r, r', \omega) = \frac{1}{U_z} \int_0^{2\pi} \int_0^{+\infty} k_R \sum_{p=-\infty}^{+\infty} \Phi_{33}(k_z, k_R, k_\gamma)$$

$$\times \exp(\mathrm{i}p(\phi_m - \phi_k)) \mathrm{J}_p(k_R r) \mathrm{J}_p(k_R r') \, \mathrm{d}k_R \, \mathrm{d}k_\gamma. \qquad (2.31)$$

This approximate expression, or the complete version in (A1), can be used in the result obtained in § 2.3 for the far-field noise spectrum (2.22) and, together with the aeroacoustic transfer functions in § 2.2, they define a complete model of turbulence ingestion noise. The exact and approximate models are named 'rotational model' and 'rotational model with untwisted blade approximation', respectively. The approximate formulation is of interest as it can speed up far-field noise predictions.

Hereafter, we consider the particular case of homogeneous isotropic turbulence. This type of idealised turbulence is advantageous because there are well-known analytical expressions for the spectrum tensor Φ_{ij}. The simplicity of the model, with only two parameters, also enables straightforward comparisons between this turbulence ingestion noise model and Amiet's model described in § 3. It does not add unnecessary layers

of complexity, when the goal of the comparison is to study other assumptions and approximations made throughout the derivations. Note, however, that in practical applications the assumption of homogeneous isotropic turbulence is not always valid. The turbulent length scales most relevant to turbulence ingestion noise generation are proportional to the radius of the rotor, and inversely proportional to the frequency of interest. The relevant wavenumber range is thus bounded by the rotor radius at low wavenumbers and the blade thickness at high wavenumbers (Simonich *et al.* 1986). Therefore, for wind turbines, for example, noise arises from very large-scale atmospheric turbulence which is unlikely to be homogeneous and isotropic. Conversely, for a cooling fan, a propeller and even a helicopter rotor, the upstream turbulence can be modelled as locally homogeneous and isotropic (Simonich *et al.* 1986). Furthermore, even in cases where the upstream turbulence is homogeneous and isotropic, rotating blades are known to distort turbulence in the streamtube on approach to the rotor disc, particularly in static conditions; see, for example, Robison & Peake (2014) and Graham (2017).

2.5. *Far-field pressure spectrum for homogeneous isotropic turbulence ingestion*

As shown earlier, in order to evaluate the turbulent velocity upwash cross-spectrum, given by (A1), one needs prior knowledge of the turbulent velocity energy spectrum. In the case of homogeneous isotropic turbulence, the energy spectrum is given by (see e.g. Christophe 2011)

$$\Phi_{ij}(k_1, k_2, k_3) = A \frac{|\hat{\boldsymbol{k}}|^2 \delta_{ij} - \hat{k}_i \hat{k}_j}{\left(1 + \hat{k}_1^2 + \hat{k}_2^2 + \hat{k}_3^2\right)^{17/6}}, \quad i, j = \{1, 2, 3\}, \quad (2.32)$$

with

$$A = \frac{55 \Gamma(5/6)\overline{u^2}}{36\pi\sqrt{\pi}\Gamma(1/3)k_e^3}, \quad k_e = \frac{\sqrt{\pi}\Gamma(5/6)}{\Lambda\Gamma(1/3)}, \quad (2.33a,b)$$

where Γ is the gamma function, δ_{ij} is the Kronecker delta and the hat denotes variables made non-dimensional with k_e. Note that $(k_1, k_2, k_3) = (k_x, k_y, k_z)$. The energy spectrum is fully characterised by the mean square of the turbulent velocity fluctuations, $\overline{u^2}$, and the turbulence integral length scale, Λ.

The energy spectrum in (2.32) can be used directly in (A1) to calculate the cross-spectrum of the blade-normal gust velocity component. Alternatively, a simpler result that is faster to compute can be obtained by substituting the energy spectrum of the streamwise turbulent velocity fluctuations given by (2.32) in (2.31) and integrating over the azimuthal wavenumber k_γ, yielding

$$S_{ww}^{(m,k)}(r, r', \omega) = \frac{2\pi A}{U_z} \int_0^{+\infty} \sum_{p=-\infty}^{+\infty} k_R \frac{\hat{k}_R^2}{\left(1 + \hat{k}_R^2 + \hat{k}_z^2\right)^{17/6}} \mathrm{J}_p(k_R r) \mathrm{J}_p(k_R r')$$

$$\times \exp(\mathrm{i}p(\phi_m - \phi_k)) \, \mathrm{d}k_R. \quad (2.34)$$

Finally, the upwash velocity cross-spectrum given in (2.34) can be substituted in (2.22) to obtain the far-field pressure spectrum at the observer location x_o as

$$
S_{pp}(x_o, \omega) = \frac{C^2 \rho^2 2\pi A}{U_z 16 R_e^2 (1 - M_z \cos\theta_e)^2} \sum_{m=0}^{B-1} \sum_{k=0}^{B-1} \sum_{n=-\infty}^{+\infty} \sum_{p=-\infty}^{+\infty}
$$

$$
\times \int_0^{+\infty} \frac{\hat{k}_R^2}{\left(1 + \hat{k}_R^2 + \left(\dfrac{\omega - (p+n)\Omega}{U_\infty k_e}\right)^2\right)^{17/6}} k_R \exp\left(\frac{\mathrm{i}2\pi(m-k)(p+n)}{B}\right)
$$

$$
\times \left| \int_{r_{hub}}^{r_{tip}} k_L U_r \mathrm{J}_n(k_r r) \mathrm{J}_p(k_R r) \mathcal{L}(\mathrm{K}_X, k_C) \exp(-\mathrm{i}\bar{k}_C)\, \mathrm{d}r \right|^2 \mathrm{d}k_R. \tag{2.35}
$$

Note that the dependence on the blade numbers m and k appears in the form $(m - k)$ and that, therefore, we need only perform the calculation for every $(m - k)$ combination. Physically, this means that the far-field pressure cross-spectrum of the noise radiated by two blades of the rotor is independent of the particular blades in question, but rather depends on their relative azimuthal position. This reduces the computational time to evaluate (2.35) significantly as only $2B - 1$ terms of the double sum over the blade numbers must be computed, instead of B^2 terms.

3. Revised Amiet's theory

In this section we re-derive the turbulence ingestion noise model of Amiet. We revisit the calculation of the time between blade chops of the same turbulent eddy as heard by the observer. This time interval fundamentally governs blade-to-blade correlation effects in the modelling strategy developed by Amiet. The present derivation will be compared to previous publications such as those of Paterson & Amiet (1979), Amiet (1989) and, more recently, Karve *et al.* (2018). In § 4, it will be shown that the revised theory yields correct predictions of haystacking tones.

3.1. *Noise radiated by aerofoil cascade in rectilinear motion*

Consider a cascade of aerofoils moving in rectilinear motion with velocity U_r at zero angle of attack, with a constant and equal offset between adjacent blades as shown in figure 2. The coordinate system (X, Y, Z) is centred mid-chord and mid-span of the zeroth aerofoil, with X in the chordwise downstream direction, Y in the spanwise direction and Z in the wall-normal direction. Let us consider a three-dimensional turbulence gust impinging on the cascade of aerofoils with its upwash velocity given by

$$
w_g(X, Y, t) = \tilde{w}_g(k_X, k_Y) \exp(\mathrm{i}[k_X(U_r t - X) + k_Y Y]). \tag{3.1}
$$

The gust–aerofoil interaction generates unsteady pressure disturbances at the surface of the aerofoil, which, in turn, radiates noise. The far-field pressure power spectral density is
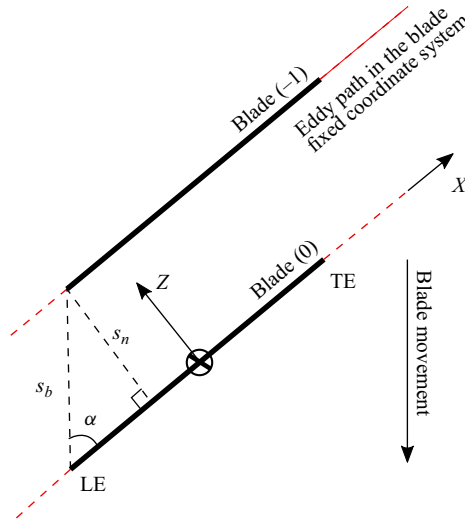
980 A53-12

Figure 2. Blade cascade diagram. Turbulent eddy path in the blade-fixed coordinate system highlighted with dashed red line. Figure adapted from Karve *et al.* (2018).

given by (Amiet 1989)

$$
S_{pp}^{(m)}(X_o, \omega) = U_r \left(\frac{k\rho Z_o b}{s_o^2} \right)^2 \int_{-\infty}^{+\infty} \int_{-\infty}^{+\infty} \Phi_{ww}(k_X, k_Y, k_Z) |\mathcal{L}_a(k_X, k_Y)|^2
$$

$$
\times \exp(-\mathrm{i} m k_Z s_n) \frac{\sin^2 \left(d \left(\frac{kY_o}{s_o} - k_Y \right) \right)}{\left(\frac{kY_o}{s_o} - k_Y \right)^2} \mathrm{d}k_Y \, \mathrm{d}k_Z, \tag{3.2}
$$

where X_o denotes the observer position in the blade-fixed coordinate system, and b and d denote the aerofoil semi-chord and semi-span, respectively. The turbulence gust streamwise wavenumber is given by $k_X = \omega/U_r$, and k_Y and k_Z denote the spanwise and wall-normal wavenumbers respectively, with all three components defined in the blade-fixed coordinate system. The amplitude radius, s_o, is approximated to zeroth order by

$$
s_o = X_o^2 + \beta_r^2 \left(Y_o^2 + Z_o^2 \right), \tag{3.3}
$$

where $\beta_r = \sqrt{1 - M_r^2}$. We have further introduced the turbulent upwash velocity spectrum in the blade-fixed coordinate system, $\Phi_{ww}(k_X, k_Y, k_Z)$, and the blade-normal distance between two consecutive blades in the unwrapped cascade, s_n, as shown in figure 2. The aeroacoustic transfer function is given by

$$
\mathcal{L}_a(k_X, k_Y) = \frac{2}{C} \int_{-C/2}^{C/2} g(X, k_X, k_Y) \exp(-\mathrm{i}\kappa (M_r - X_0/s_o) X) \, \mathrm{d}X. \tag{3.4}
$$

Equation (3.4) differs from that introduced in § 2.2 in that it accounts for three-dimensional turbulence gusts. A detailed derivation of the aeroacoustic transfer function in the high-frequency regime can be found in Appendix C.1 of Christophe (2011). For frequencies where the blade chord is compact we require another solution that is valid

in the low-frequency regime, i.e. for $\omega C/2c_0(1 - M_r^2) < \pi/4$ (Amiet 1975). In this case, we use the aerofoil transfer function given by Amiet (1989).

The far-field noise power spectral density given by (3.2) is further simplified if we consider an infinite-span aerofoil, in which case

$$S_{pp}^{(m)}(X_o, \omega) = \left(\frac{k\rho Z_o b}{s_o^2}\right)^2 \pi \, \mathrm{d}U_r \int_{-\infty}^{+\infty} \Phi_{ww}(k_X, k_Y, k_Z)|\mathcal{L}_a(k_X, k_Y)|^2$$
$$\times \exp(-\mathrm{i}mk_Z s_n) \, \mathrm{d}k_Z, \tag{3.5}$$

where the spanwise wavenumber is now given by $k_Y = kY_o/s_o$.

3.2. *Blade-to-blade correlation*

In § 3.1, we considered the noise generated by a single blade in rectilinear motion. In this section, we incorporate the effects of noise source correlation between blades in the far-field noise prediction. These effects are more prominent when consecutive blades chop the same turbulent eddy as it travels through the rotor. This equates to satisfying the condition $B\Omega \Lambda/U_z \gg 1$ (Glegg *et al.* 2012; Glegg & Devenport 2017).

3.2.1. *Time between blade chops*

Of particular importance to the model developed by Amiet (1989) is the time, as seen by the observer, between blade chops. Figure 2 is particularly useful to a physical understanding of the quantities involved. The blade-normal distance between two blades is given by

$$s_n = s_b \sin \alpha. \tag{3.6}$$

The reader is reminded that $U_r = \sqrt{U_z^2 + U_\gamma^2}$ is the blade relative velocity, where U_z is the axial flow velocity and $U_\gamma = \Omega r$ is the tangential velocity. The distance between two consecutive blades in the unwrapped azimuthal direction can be expressed in terms of the velocity in this direction, U_γ, and the blade-passage time $T_B = 2\pi/B\Omega$, as

$$s_b = U_\gamma T_B. \tag{3.7}$$

Substituting (3.7) in (3.6) and knowing that $\sin \alpha = U_z/U_r$ yields

$$s_n = \frac{U_\gamma U_z T_B}{U_r}. \tag{3.8}$$

The time between eddy chops is the time it takes for the wavefront of an eddy to travel from the leading edge of the first blade to the leading edge of the second blade. From figure 2, this distance is given by $s_b \cos \alpha$. Moreover, in the blade-fixed coordinate system the turbulent eddy travels in the downstream direction with velocity U_r. The time between eddy chops is thus given by

$$T_C = \frac{s_b \cos \alpha}{U_r}, \tag{3.9}$$

which, using (3.7), equates to

$$T_C = \frac{U_\gamma^2 T_B}{U_r^2}. \tag{3.10}$$

We must now calculate the time between blade chops from the perspective of the observer. Let us denote by $\tau^{(0)}$ and $\tau^{(-1)}$ the time taken for the acoustic waves to travel from blade

0 and blade -1 to the observer, respectively. The time between blade chops as seen by the observer, T_O, can then be expressed as

$$T_O = T_C + \tau^{(-1)} - \tau^{(0)}. \tag{3.11}$$

The time for sound waves to travel from the zeroth blade to the observer is, by definition, given by the phase radius divided by the speed of sound (Garrick & Watkins 1953). Approximating the phase radius by retaining the zeroth-order terms of its Taylor expansion about the origin of the coordinate system yields

$$\tau^{(0)} = \frac{s_o - M_r X_o}{\beta_r^2 c_0}, \quad \tau^{(-1)} = \frac{s'_o - M_r X'_o}{\beta_r^2 c_0}, \tag{3.12a,b}$$

where the dash indicates observer coordinates measured in the coordinate system (X', Y', Z') centred mid-chord and mid-span of blade -1. The relationship between the two sets of coordinates, expressed in vectorial form as X_o and X'_o, is expressed as

$$X_o = X'_o + X_{BB}, \tag{3.13}$$

where the separation between the two blades, as seen from figure 2, is given by

$$X_{BB} = \left[\sqrt{s_b^2 - s_n^2}, 0, s_n \right]^{\mathrm{T}}. \tag{3.14}$$

We now turn to the calculation of $\tau^{(-1)}$. The first step is to develop the amplitude radius s'_o, given by

$$s'_o = \sqrt{X_o'^2 + \beta_r^2 \left(Y_o'^2 + Z_o'^2 \right)}, \tag{3.15}$$

which after change of variables using (3.13) and Taylor expansions, retaining terms up to first order, yields

$$s'_o = s_o - \frac{U_\gamma T_B}{U_r s_o} \left(X_o U_\gamma + \beta_r^2 U_z Z_o \right). \tag{3.16}$$

This result allows us to readily calculate $(\tau^{(-1)} - \tau^{(0)})$ from (3.12) and (3.13) as

$$\tau^{(-1)} - \tau^{(0)} = \frac{U_\gamma T_B}{U_r s_o \beta_r^2 c_0} \left[U_\gamma \left(M_r s_o - X_o \right) - \beta_r^2 U_z Z_o \right]. \tag{3.17}$$

The time between blade chops as seen by the observer, T_O, can finally be evaluated by (3.11), together with (3.10) and (3.17). This is one of the key contributions of this paper.

3.2.2. *Comparison with previous works*

Let us compare (3.17) with the equivalent results of Paterson & Amiet (1979), Amiet (1989) and Karve *et al.* (2018). Paterson & Amiet (1979) concluded that the time between blade chops as seen by the observer is given by $T_O = T_C$ and, thus, neglected the time difference that the acoustic waves take to propagate from each blade to the observer given here by (3.17). Amiet (1989) extended the model of Paterson & Amiet (1979) to consider this aspect of the problem. In that report, the authors arrived at the following result for the acoustic wave propagation time difference

$$\tau^{(-1)} - \tau^{(0)} = \frac{|\Delta X_o|}{\beta_r^2 c_0 s_o} \left(s_o M_r - X_o \right), \tag{3.18}$$

where $|\Delta X_o| = U_z^2 U_\gamma T_B / U_r^2$. This is in disagreement with our own calculation in (3.17). No clear derivation was presented, although it appears the authors have sought to consider

the assumed rectilinear movement of the blades relative to the observer during the time between blade chops. In our derivation, this would manifest as an additional term in (3.13). Although in the first instance this seems to be a reasonable approach, it conflicts with the implicit assumption made in § 3.1 that the observer is fixed with respect to the cascade of aerofoils. The relative motion between the two is only addressed in § 3.3.

More recently Karve *et al.* (2018) presented their own result for the time between blade chops as heard by the observer. However, no detailed derivation was presented. Their result for the acoustic wave propagation time difference is given by

$$\tau^{(-1)} - \tau^{(0)} = \frac{-U_\gamma U_z T_B Z_o}{U_r c_0 s_o}, \tag{3.19}$$

which is equal to the second term of the result presented in this paper in (3.17). The authors appear to have only accounted for one of the components in the blade offset vector X_{BB}. However, their overall approach of considering a fixed observer with respect to the cascade of aerofoils is in agreement with the present approach, while contrasting with that of Amiet (1989). In § 4, we show numerical evidence that both their result and that of Amiet (1989) lead to incorrect far-field pressure power spectral densities, failing to predict haystacking tones which are a prominent feature of turbulence ingestion noise spectra.

3.2.3. *Far-field pressure spectrum*
Paterson & Amiet (1979) argued that the far-field autocorrelation function consists of a series of peaks, where the mth peak represents the correlation between the noise originating in the zeroth blade and the noise originating in the mth blade. Mathematically, this is represented as

$$R_{pp}(X_o, t) = \sum_{m=-\infty}^{+\infty} R_{pp}^{(m)}(X_o, t + mT_O), \tag{3.20}$$

where $R_{pp}^{(m)}$ denotes the cross-correlation between the far-field pressure generated by the zeroth and the mth blade, and T_O is the time between blade chops as heard by the observer given by (3.11). The far-field pressure spectrum is obtained by taking the Fourier transform, yielding

$$S_{pp}(X_o, \omega) = \sum_{m=-\infty}^{+\infty} S_{pp}^{(m)}(X_o, \omega) \exp(im\omega T_O), \tag{3.21}$$

where $S_{pp}^{(m)}(X_o, \omega)$ is given by (3.5) or (3.2), with and without an infinite-span wing assumption, respectively. Substituting (3.5) in (3.21), we obtain

$$S_{pp}(X_o, \omega) = \sum_{m=-\infty}^{+\infty} \left(\frac{k\rho Z_o b}{s_o^2}\right)^2 \pi U_r d \int_{-\infty}^{+\infty} \Phi_{ww}(k_X, k_Y, k_Z)|\mathcal{L}_a(k_X, k_Y)|^2$$
$$\times \exp(im(-k_Z s_n + \omega T_O)) \, \mathrm{d}k_Z. \tag{3.22}$$

Using the delta Dirac train identity

$$\sum_{m=-\infty}^{+\infty} \exp(i2\pi m a) = \sum_{m=-\infty}^{+\infty} \delta(m - a), \tag{3.23}$$

we obtain

$$S_{pp}(X_o, \omega) = \left(\frac{k\rho Z_o b}{s_o^2}\right)^2 \frac{2\pi^2 U_r d}{s_n} |\mathcal{L}_a(k_X, k_Y)|^2 \sum_{m=-\infty}^{+\infty} \Phi_{ww}(k_X, k_Y, k_Z), \qquad (3.24)$$

where $k_X = \omega/U_r$, $k_Y = kY_o/s_o$ and $k_Z = (\omega T_O - 2\pi m)/s_n$. Alternatively, if blade-to-blade correlation effects are negligible, i.e. if the condition $(B\Omega \Lambda/U_z) \gg 1$ is not respected (Glegg *et al.* 2012; Glegg & Devenport 2017), the far-field power spectral density is simply given by (3.5) with $m = 0$.

For homogeneous isotropic turbulence, the full energy spectrum is given by (2.32). The turbulence upwash velocity spectrum in the blade-fixed coordinate system is readily obtained by considering that isotropic turbulence has invariant properties under rotation,

$$\Phi_{ww}(k_X, k_Y, k_Z) = A \frac{\hat{k}_X^2 + \hat{k}_Y^2}{\left(1 + \hat{k}_X^2 + \hat{k}_Y^2 + \hat{k}_Z^2\right)^{17/6}}, \qquad (3.25)$$

where A is given by (2.33).

3.3. *Noise radiated by rotating blades*

The far-field pressure spectrum in (3.24) corresponds to the noise generated by a cascade of aerofoils in rectilinear motion. In the context of Amiet's theory (Amiet 1989), thoroughly and clearly described in Sinayoko *et al.* (2013), it represents an approximation to the instantaneous power spectral density generated by a strip of rotating blades at a given azimuthal angle. Amiet argued that this is a suitable approximation when the source frequency is much larger than the rotor angular velocity, i.e. $\omega \gg \Omega$. Obtaining the total far-field pressure spectrum requires:

(i) applying a Doppler effect correction to account for the movement of the observer relative to the blade;
(i1) averaging the instantaneous power spectral density over all azimuthal angles;
(iii) summing the contributions of each blade strip.

Sinayoko *et al.* (2013) provides a complete description of steps (i) and (ii), which we will not reproduce here. A summary of the key results is given instead. Step (iii) alludes to the use of strip theory, where rotor blades are divided into small strips and the total far-field power spectral density is given by the sum of the individual, uncorrelated contributions of each strip.

The time-averaged power spectral density from the *j*th strip element of rotating blades is given by (Sinayoko *et al.* 2013)

$$S_{pp}^{(j)}(\boldsymbol{x}_o, \omega) = \frac{1}{2\pi} \int_0^{2\pi} \left(\frac{\omega'}{\omega}\right)^2 S_{pp}^{(j)}(X_o, \omega', \gamma) \, d\gamma, \qquad (3.26)$$

where $S_{pp}^{(j)}(X_o, \omega', \gamma)$ is the power spectral density given by (3.24) or (3.5), for cases with or without blade-to-blade correlation effects, respectively. We have now made the power spectral density an explicit function of the azimuth angle and the blade strip number; the latter serves to acknowledge the dependence of the results obtained in § 3.2.3 on the radial

position as a result of varying geometric properties and flow conditions. The factor ω'/ω is the Doppler-shift correction for each azimuth angle and each blade strip, as given by

$$\frac{\omega}{\omega'} = 1 + \frac{M_{BO} \cdot \widehat{CO}}{1 + (M_{FO} - M_{BO}) \cdot \widehat{CO}}, \tag{3.27}$$

where M_{BO} and M_{FO} are the blade and fluid Mach number vectors relative to the observer,

$$M_{BO} = \left[-M_\gamma \sin\gamma, M_\gamma \cos\gamma, 0\right]^{\mathrm{T}}, \quad M_{FO} = \left[0, 0, -M_z\right]^{\mathrm{T}}, \tag{3.28a,b}$$

where $M_\gamma = U_\gamma/c_o$, and $\widehat{CO}$ is the unit vector from the convected source position, x_c, to the observer position, x_o,

$$\widehat{CO} = \frac{x_o - x_c}{|x_o - x_c|}, \tag{3.29}$$

with $x_c = M_{FO}R_p$. The propagation distance, R_p, is, in turn, given by

$$R_p = \frac{|x_o|\left(-|M_{FO}|\cos\Theta + \sqrt{1 - |M_{FO}|^2 \sin^2\Theta}\right)}{1 - |M_{FO}|^2}, \tag{3.30}$$

where Θ denotes the angle between M_{FO} and x_o. It remains to calculate the observer position in the blade-fixed coordinate system X_o. From Sinayoko *et al.* (2013), we know that

$$X_o = \underline{R}_y(\alpha)\underline{R}_z(\pi/2 - \gamma)\left(x_o - x_p\right), \tag{3.31}$$

where $\underline{R}_y$ and $\underline{R}_z$ are rotation matrices given by

$$\underline{R}_z(\theta) = \begin{pmatrix} \cos\theta & -\sin\theta & 0 \\ \sin\theta & \cos\theta & 0 \\ 0 & 0 & 1 \end{pmatrix}, \quad \underline{R}_y(\theta) = \begin{pmatrix} \cos\theta & 0 & -\sin\theta \\ 0 & 1 & 0 \\ \sin\theta & 0 & \cos\theta \end{pmatrix}, \tag{3.32a,b}$$

and x_p is the present source position, approximated by

$$x_p = M_{BO}R_p. \tag{3.33}$$

We now have all the information to calculate (3.26). It remains to sum up the power spectral density contributions of each blade strip. The blades are divided into N_s segments following a logarithmic distribution with clustering in the blade tips. The flow and geometric quantities of each strip needed to calculate the far-field pressure spectrum are given by their values at the centre of the strip. The total power spectral density is then given by the sum of the individual contributions in (3.26), as

$$S_{pp}(x_o, \omega) = B\sum_{j=1}^{N_s} S_{pp}^{(j)}(x_o, \omega). \tag{3.34}$$

4. Results and discussion

In this section we compare the model for turbulence ingestion noise presented in § 2 with the derivation of Amiet's theory presented in § 3, and validate both models through comparisons with experimental data. The two turbulence ingestion noise models differ in several aspects. The new formulation takes into account the rotational motion of the blades, whereas Amiet's theory assumes that, on the time scales of noise radiation, the blades can

be considered to be in rectilinear motion ($\omega \gg \Omega$). In addition, the model presented in this paper includes the cross-correlation between the sound pressure generated at different radial segments of the blade. In contrast, Amiet's theory relies on strip theory with an infinite-span assumption to calculate the total far-field spectrum as the sum of uncorrelated contributions from each blade strip. The main drawback of the rotational formulation as compared with Amiet's theory is that three-dimensional gusts are not considered, although it is precisely this feature of the model that ultimately enables the analytical calculation of cross-correlations across the blade span. We proceed to study the effect of this assumption on far-field noise predictions for a stationary aerofoil before comparing the rotational formulation against Amiet's theory for rotating blades.

4.1. *Effects of two-dimensional turbulent flow approximation in stationary aerofoil*

Let us consider a stationary aerofoil with a flat-plate geometry of span $2d$ and chord $2b$ in a uniform flow of velocity U_r at zero angle of attack. The far-field pressure power spectral density for observer coordinates $X_o = (0, 0, Z_o)$ under a two-dimensional turbulent flow approximation is given by

$$S_{pp}(X_o, \omega) = \left[\frac{kZ_o\rho b}{2s_o^2}\right]^2 U_r |\mathcal{L}_a(k_X, 0)|^2 \int_{-d}^{d} \int_{-d}^{d} \Theta_{ww}(\delta Y, k_X = \omega/U_r)\, dY\, dY', \quad (4.1)$$

with $\Theta_{ww}(\delta Y, \omega/U_r)$ denoting the one-dimensional upwash velocity cross-spectra as a function of the spanwise spatial separation $\delta Y = Y - Y'$. It is given by (see e.g. Wilson 1997)

$$\Theta_{ww}(\delta Y, \omega/U_r) = \frac{2^{1/6}\overline{u^2}}{\sqrt{\pi}k_e\Gamma(1/3)} \left(\frac{\xi}{1+\bar{\omega}^2}\right)^{5/6} \left[\frac{4}{3}K_{5/6}(\xi) - \frac{\xi}{2(1+\bar{\omega}^2)}K_{11/6}(\xi)\right], \quad (4.2)$$

where $\xi^2 = k_e^2 \delta Y^2 (1 + \bar{\omega}^2)$, $\bar{\omega} = \omega/(k_e U_r)$ is the reduced frequency and K_ν is the modified Bessel function of the second kind of order ν.

In figure 3(*a*) the new formulation given by (4.1) ('2-D – finite-span') is compared with Amiet's theory with and without an infinite-span assumption ('3-D – infinite-span' and '3-D – finite-span'), as given by (3.5) and (3.2), respectively. Power spectral density predictions by these three formulations are compared for a flat-plate of chord 0.3 m and span 1.5 m within homogeneous isotropic turbulence with turbulence intensity $\sqrt{\overline{u^2}}/U_r = 0.05$ and length scale $\Lambda = 0.1$ m, and in a uniform flow ($M_r = 0.6$). The observer is positioned overhead in the centreline plane, with coordinates $(X_o, Y_o, Z_o) = (0, 0, 200d)$. The reference pressure is $p_{ref} = 2 \times 10^{-5}$ Pa.

We observe excellent agreement at reduced frequencies higher than $kC \approx 0.5$. The assumptions of infinite-span and two-dimensional flow begin to break down for frequencies lower than this value. The two-dimensional turbulent flow approximation tends to result in an overestimate of the power spectral density because every spanwise wavenumber is considered to radiate as efficiently as a two-dimensional gust. In other words, (2.10) lumps together the contributions of all spanwise wavenumbers into the point spectrum $\tilde{w}_g(\omega)$ without accounting for the fact that the aerofoil response function varies with the turbulent gust spanwise wavenumber. This can be shown to fully explain the difference in results between the finite-span formulation of Amiet and the two-dimensional approximation derived in this section by forcing $\mathcal{L}_a(k_X, k_Y) = \mathcal{L}_a(k_X, 0)$ in Amiet's formulation given by (3.2) (not shown here).
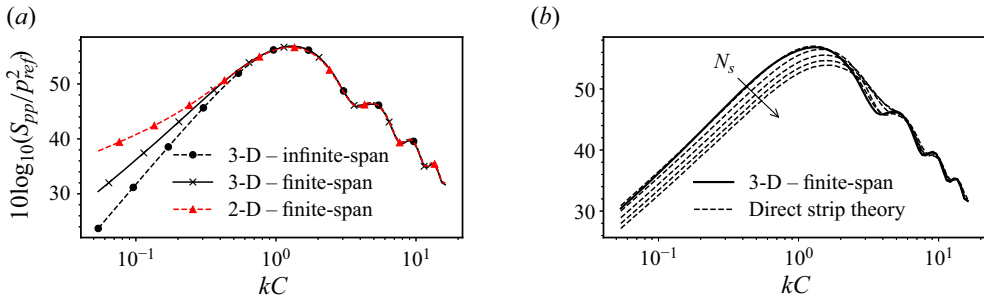
Figure 3. Far-field pressure power spectral density for a stationary flat-plate geometry ($2b = 0.3$ m, $2d = 1.5$ m) within homogeneous isotropic turbulence with turbulence intensity $\sqrt{\overline{u^2}}/U_r = 0.05$ and length scale $\Lambda = 0.1$ m, and in a uniform flow ($M_r = 0.6$). Observer is positioned overhead in the centreline plane, $(X_o, Y_o, Z_o) = (0, 0, 200d)$. (*a*) Comparing Amiet's theory with and without infinite-span assumption ('3-D – infinite-span' and '3-D – finite-span', respectively), and two-dimensional approximation ('2-D – finite-span'). (*b*) Comparing Amiet's finite-span theory with direct strip theory based on the same formulation.

Figure 3(*b*) illustrates the use of strip theory based on Amiet's finite-span formulation (3.2) with N_s strips, where N_s varies between 2 and 10 in increments of 2. As can be seen, the results do not converge when increasing the number of strips, particularly at low reduced frequencies. It can be shown that the difference between the finite-span formulation and the results of applying strip theory is exclusively due to neglecting cross-spectrum contributions between strip elements. Note that the two-dimensional formulation in (4.1), and its equivalent for rotating blades found in § 2, account for this; these formulations lend themselves to strip theory more naturally as the total noise appears as an integral of the contributions along the spanwise or radial directions. As such, its results in figure 3(*a*) ('2-D – finite-span') are comparable to the results of strip theory in figure 3(*b*) when considering the stationary aerofoil as a simple test subject of the methodology that is applied to a rotating blade. In the case of rotating blades a 'true' solution such as the '3-D – finite-span' line is not available, and only stripping methods can be used.

When applying these methods to rotors, there is a need to discretise the blades into a large number of thin strips to capture changes in geometry and flow conditions in the radial direction. Figure 3(*b*) shows that refining the blade discretisation is problematic because the far-field spectrum becomes increasingly under-predicted at lower frequencies. To remove the arbitrary choice of the number of strips, N_s, it is often the case that an infinite-span assumption is made for each strip (as in (3.5) and (3.24)). This results in predictions which do converge with the number of strips. In the case of a stationary aerofoil, the result is even invariant with respect to the number of strips and equal to the result shown in figure 3(*a*) with the label '3-D – infinite-span'. The infinite-span simplification is based on the argument that each blade strip should be wider than the turbulence correlation length scale. However, this justification cannot hold valid for all frequencies, nor is it necessarily compatible with the need to discretise the blade in such a way as to capture changes in geometry and flow conditions.

4.2. *Definition of rotating blade test cases*

We define three test cases in table 1 to evaluate the turbulence ingestion noises models derived in this paper. These test cases were initially proposed by Blandeau & Joseph (2011) and used by Sinayoko *et al.* (2013) in their studies of trailing-edge noise. They are chosen

980 A53-20

	Cooling fan	Open propeller	Wind turbine
C (m)	0.13	0.31	2
r_{tip} (m)	0.4	1.8	29
RPM (s^{-1})	600	1800	25
M_z	0.0354	0.229 (take-off)	0.029
B	2	6	3
$B\Omega C/(2c_0(1 - M_r^2))$	0.023	64.5	0.024

Table 1. Typical parameters for different types of rotors proposed by Blandeau & Joseph (2011).

to represent a wide range of potential applications. It is worth noting that the present turbulence ingestion noise models were derived under the assumption of a rigid blade. This approximation is especially of concern for wind turbines and should be investigated if the models are to be used for rotors where blade flexibility is significant. One simple approach would be to consider the sensitivity of the results to considering the deflected blade geometry as opposed to the rigid blade geometry. This is a topic of future research.

The angle of attack is zero across all cases and, thus, the pitch angle is governed by (2.1). We further define the hub radius as $r_{hub} = 0.1r_{tip}$. The observer is positioned in the plane of the rotor, at $(x_o, y_o, z_o) = (20r_{tip}, 0, 0)$. The turbulence intensity is equal to $\sqrt{\overline{u^2}}/U_z = 0.075$ and the turbulence length scale is such that the non-dimensional parameter governing blade–blade interactions is constant, $B\Omega \Lambda/U_z = 4$. This ensures that haystacking around the blade-passing frequencies will be a prominent feature of the power spectral densities (Glegg *et al.* 2012; Glegg & Devenport 2017).

In the last row of table 1 we assess the criterion $\omega C/2c_0(1 - M_r^2) < \pi/4$, which defines the changeover between the two frequency regimes of the aeroacoustic transfer function. The values are calculated at the blade tip radius for $\omega = 2\pi B\Omega$. This serves as an indicator of the frequency regime of each test case. Based on this criterion, we choose to use the high-frequency aeroacoustic transfer function for the open propeller, and the Sears response function for the cooling fan and wind turbine.

4.3. *Turbulent upwash velocity cross-spectrum comparisons*

In this section we assess the untwisted blade approximation introduced in § 2.4 by evaluating the turbulent upwash velocity cross-spectrum for each test case in its exact and approximate forms. The approximate formulation is of interest as it can speed up far-field noise predictions. Its faster runtime is mainly due to the simplification of the double integral in the radial direction (see (2.22)) to a single integral (see (2.35)). This speedup is not restricted to the case of homogeneous isotropic turbulence. The approximate formulation is also beneficial in cases where experimental data are used to directly calculate the upwash velocity cross-spectrum through (2.26), both because the evaluation of the expression is less costly, and because the experimental apparatus can be simplified if only one velocity component needs to be measured.

Figure 4 presents the exact evaluation of the upwash velocity cross-spectrum using (A1), as well as an approximate solution given by (2.31), where the blade pitch angle is assumed to be zero. We chose to present the auto-spectrum at the blade root ($r = r' = r_{hub}$) and the blade tip ($r = r' = r_{tip}$), and the cross-spectrum at the tips of two consecutive blades (designated 'cross-blade tip'). The latter was chosen because blade-to-blade correlation is the cause of the haystacking phenomenon.
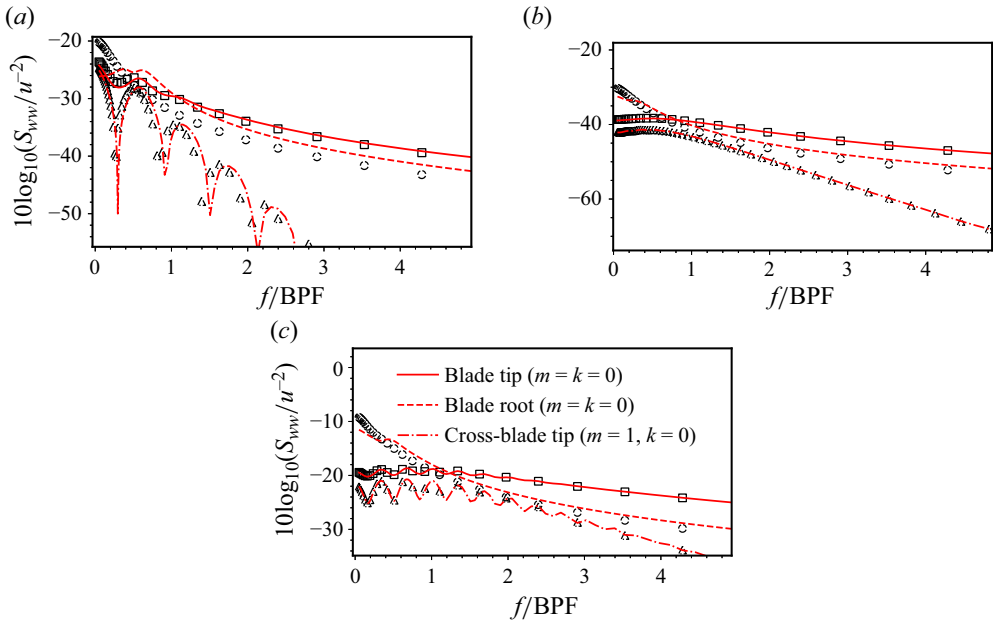
Figure 4. Exact upwash velocity power spectral density given by (A1) for homogeneous isotropic turbulence at blade tip ($r = r' = r_{tip}$) [thick solid red line], blade root ($r = r' = r_{hub}$) [thick dashed red line] and cross-blade tip ($r = r' = r_{tip}$) [thick dash-dotted red line]. The black hollow markers show the approximate upwash velocity power spectral density given by (2.31) at each radial distance. (*a*) Cooling fan, (*b*) open propeller and (*c*) wind turbine.

As can be seen from the results in figure 4, generally good agreement is found between the full and approximate evaluations of the upwash velocity cross-spectrum for the cooling fan, open propeller and wind turbine, thus showing the robustness of this approximation. Exceptionally good agreement is observed in the open propeller and wind turbine cases. The analysis in § 2.4 shows that the untwisted blade approximation should be more accurate for rotors operating at low advance ratios. Therefore, the better agreement observed in the case of the open propeller and wind turbine is to be expected since they operate at advance ratios $J = 0.74$ and $J = 0.42$, respectively, whereas the cooling fan operates at $J = 1.55$. It is further observed that in all three cases agreement deteriorates when considering the auto-spectrum at the blade root. This is an anticipated behaviour since the blade pitch angle increases with decreasing radial position.

4.4. *Far-field noise comparisons*

In this section we compare the turbulence ingestion noise model presented in this paper with Amiet's theory for rotating blades. For clarity, the equations used in each model are summarised as follows.

(i) **Rotational model**: far-field spectrum is given by (2.22), where the upwash velocity cross-spectrum is determined by (A1) using the homogeneous isotropic turbulence spectrum in (2.32) as an input. This model is referred to as the rotational model.

(ii) **Rotational model with untwisted blade approximation**: the far-field spectrum is given by (2.35), which was derived from the rotational model by introducing an untwisted blade approximation. In what follows, we refer to this model as the rotational model with untwisted blade approximation.
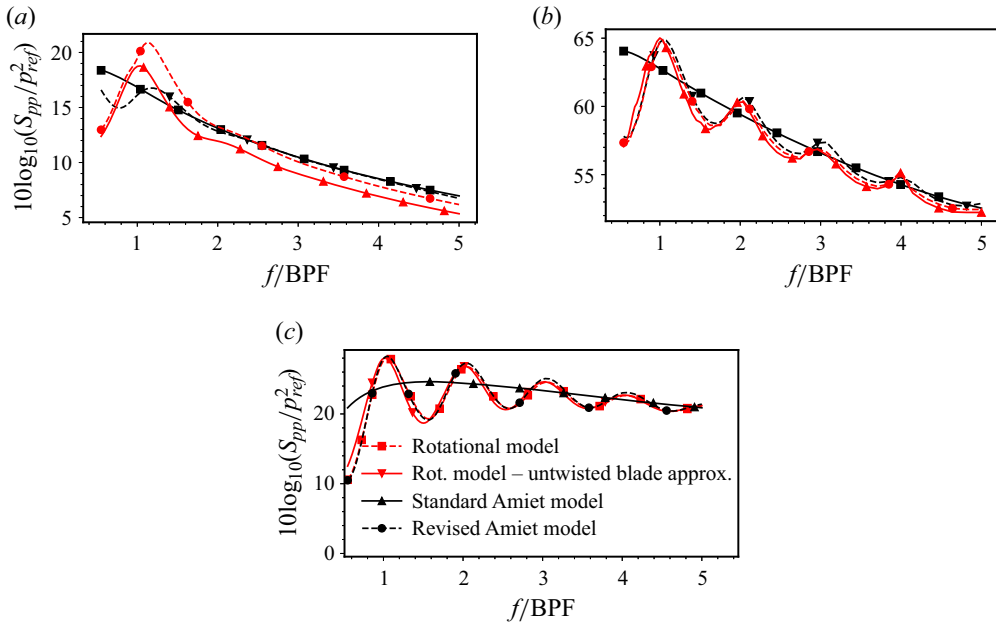
Figure 5. Far-field pressure power spectral density for three different types of rotors. (*a*) Cooling fan with Sears response function, (*b*) open propeller with first-order high-frequency aeroacoustic transfer function and (*c*) wind turbine with Sears response function. Comparison between the rotational model in §2 and Amiet's theory in §3. Each model is summarised in §4.4.

  (iii) **Amiet's model**: the far-field spectrum in (3.34) is given by the uncorrelated sum of each strip's contribution as calculated by (3.26), where the noise produced at each azimuthal position is given by (3.5) with $m = 0$ for cases without blade-to-blade correlation effects. This model is referred to as the standard Amiet model.

  (iv) **Amiet's model with blade-to-blade correlation**: the inclusion of blade-to-blade correlation effects requires only replacing (3.5) in Amiet's model with (3.24). In the rest of the paper, we refer to this model as the revised Amiet model.

Both the rotational model and Amiet's theory for rotating blades have the option of using a high-frequency approximation to the aeroacoustic transfer function (with or without a back-scattering correction) or a Sears response function.

The numerical evaluation of these equations is straightforward but it is important to make sure that the results are converged with respect to several parameters. For Amiet's model, attention is paid to the number of blade strips, the number of azimuthal points and the number of blade-to-blade interactions (i.e. truncation of the sum in (3.24)). For the rotational model, we consider the number of points in the radial discretisation of the blade; the number of terms in the infinite series involving Bessel functions; and the size and discretisation of the domain of integration over the radial wavenumber.

In figure 5 we compare the power spectral density prediction of the four models described previously for the three test cases summarised in table 1. There is excellent agreement between the revised Amiet model and the rotational model across the three test cases. Agreement is particularly exceptional for the open propeller and wind turbine. Both models capture the energy haystacking around multiples of the blade-passing frequency (20 Hz, 180 Hz and 1.25 Hz for the cooling fan, open propeller and wind turbine, respectively). The results of the standard Amiet model are presented for reference.
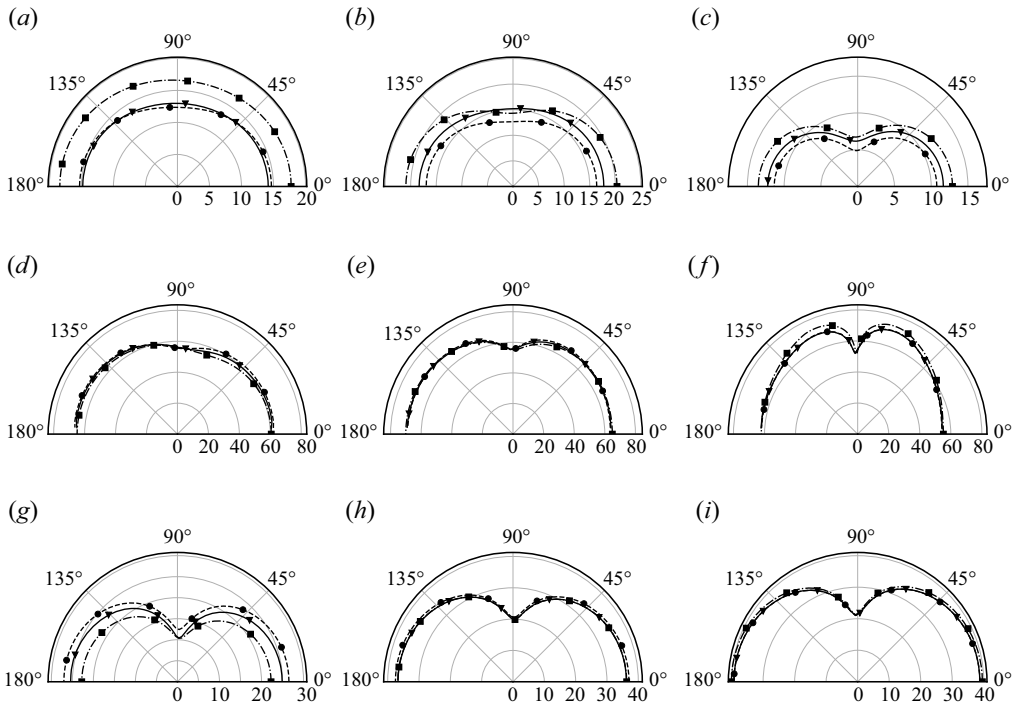
980 A53-23

Figure 6. Far-field pressure power spectral density ($10\log_{10}(S_{pp}/p_{ref}^2)$) directivity ($0°$ corresponds to an observer position downstream of the propeller) in the mid-plane ($y_o = 0$) for fixed observer distance ($|x_o| = 20r_{tip}$). Comparison between the revised Amiet model (–·– · ■), rotational model (—— ▼) and rotational model with untwisted blade approximation (- - - ●). Sears response function used throughout all computations. First row, cooling fan; second row, open propeller; third row, wind turbine. First column, $f/\text{BPF} = 0.55$; second column, $f/\text{BPF} = 1.66$; third column, $f/\text{BPF} = 5.0$.

Comparison with the other models shows that blade-to-blade correlation leads to a redistribution of energy, with concentration around the blade-passing frequencies.

Considering the differences between the rotational model with an untwisted blade approximation and the full model leads to the same conclusions drawn in the previous section where the upwash velocity cross-spectrum was examined. Generally good agreement is found across all test cases, but the approximation is more precise for the open propeller and wind turbine which operate at lower advance ratios. For the cooling fan, differences are under 3.2 dB. It is also in this test case that we observe the largest differences between the rotational model and the revised Amiet model. This appears to be unrelated to rotational effects since the ratio ω/Ω is similar for the wind turbine and yet no differences are observed in this case. We hypothesise that it is related to the relative size of turbulence length scale to the rotor blades. This ratio, Λ/r_{tip}, is approximately 1 for the cooling fan and approximately 0.2 for the other test cases. Large spanwise correlation lengths run contrary to the assumption in Amiet's theory that each strip can be modelled independently, without accounting for noise source correlation across the span of the blade. This aspect is further investigated in § 4.4.1.

Figure 6 compares the power spectral density directivity in the propeller mid-plane ($y_o = 0$) as predicted by the revised Amiet model and the rotational model, in its full and approximate forms, for the three test cases summarised in table 1. Note that the Sears response function was used in all computations here, including the open propeller. This
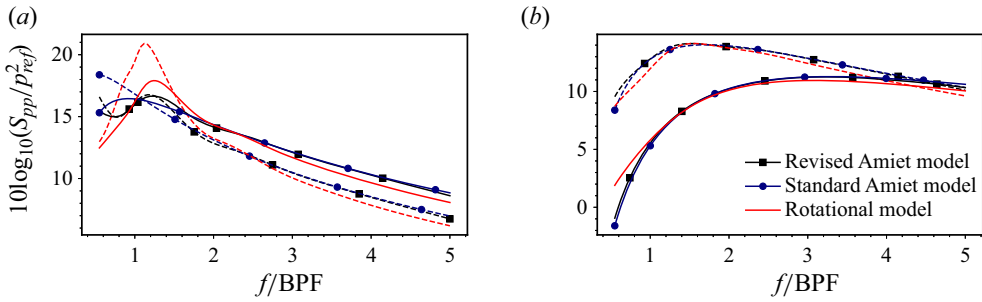
980 A53-24

Figure 7. Effect of turbulence length scale on the far-field pressure power spectral density of the cooling fan: (a) $B\Omega\Lambda/U_z = 4$ (---) and $B\Omega\Lambda/U_z = 2$ (——); (b) $B\Omega\Lambda/U_z = 1$ (---) and $B\Omega\Lambda/U_z = 0.5$ (——). The colours and markers in the legend distinguish between the different models.

is because, as seen from figure 5(b), the power spectral density can be very 'peaky' near exact multiples of the propeller angular velocity. The reason for this is that the first-order high-frequency approximation to the aeroacoustic response function in (2.14) tends to infinity when $\omega \to 0$; from (2.35), and knowing that $K_X = (\omega - n\Omega)/U_r$, it can be seen that this causes the power spectral density to tend to infinity too. The immediate conclusion from this observation is that the high-frequency approximation to the aeroacoustic response function alone cannot be used in the rotational model. Either a uniformly valid response function (Posson, Moreau & Roger 2010) or a composite asymptotic approximation should be used instead in order to model the full range of frequencies. This aspect merits further investigation but it is beyond the scope of this paper.

The results in figure 6 show the expected dipole directivity pattern of turbulence ingestion noise. The comparison between the three models at different observer polar angles reinforces the conclusions drawn from the spectrum at single observer position: (i) the untwisted blade approximation is more precise for the open propeller and wind turbine which operate at lower advance ratios; (ii) the revised Amiet model is in good agreement with the rotational model.

4.4.1. *Isotropic turbulence length scale*

We now focus on the effects of varying the isotropic turbulence length scale. We restrict our attention to the cooling fan and the wind turbine. The power spectral density spectrum is shown in figures 7 and 8, respectively, for the parameters $B\Omega\Lambda/U_z = \{0.5, 1.0, 2.0, 4.0\}$. It is observed that Amiet's standard and revised models tend to be in good agreement when the turbulence length scale decreases such that no haystacking is present. In the case of wind turbine, very good agreement is found between the rotational model and Amiet's theory for all turbulence length scales. Crucially, in the case of the cooling fan, reduced turbulence length scales lead to improved agreement in the low-frequency region of the spectrum. This supports our earlier hypothesis that the poor agreement in figure 5(a) around $f/BPF = 1$ when $B\Omega\Lambda/U_z = 4$ was related to the relative size of turbulence length scale to the rotor blades. Amiet's theory relies on strip theory to calculate the total far-field spectrum as the sum of uncorrelated contributions from each blade strip. Therefore, it is expected that it should lose accuracy for larger ratios of Λ/r_{tip}, i.e. when the turbulent eddies are correlated over a larger portion of the blade.
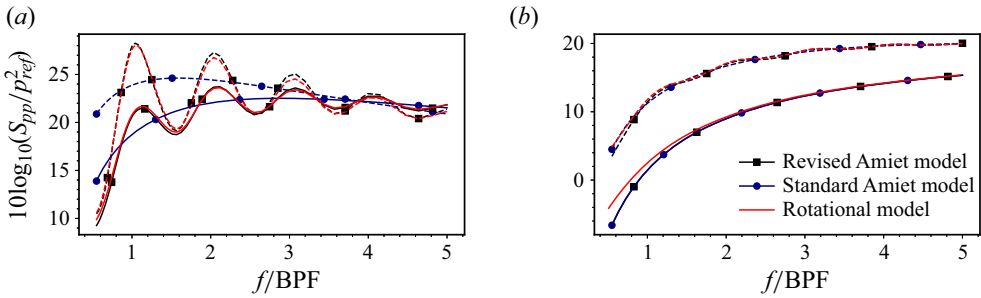
980 A53-25

Figure 8. Effect of turbulence length scale on the far-field pressure power spectral density of the wind turbine: (*a*) $B\Omega\Lambda/U_z = 4$ (---) and $B\Omega\Lambda/U_z = 2$ (——); (*b*) $B\Omega\Lambda/U_z = 1$ (---) and $B\Omega\Lambda/U_z = 0.5$ (——). The colours and markers in the legend distinguish between the different models.
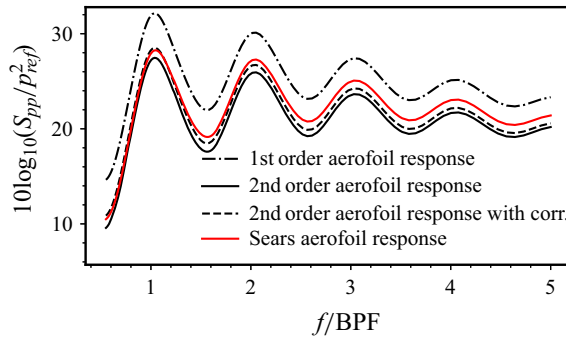

Figure 9. Far-field pressure power spectral density for wind turbine using different models of aeroacoustic transfer function. High frequency first- and second-order transfer functions given by (2.14) and (2.16). Correction to back-scattering component found in Santana *et al.* (2016). Sears response function given by (2.20). Computations carried out with the revised Amiet model.

4.4.2. *Aeroacoustic transfer function*

We investigate how the choice of aeroacoustic transfer function affects the predictions of the far-field pressure power spectral density. In § 2.2 of this paper, we have used first- and second-order high-frequency successive approximations (i.e. Amiet's aerofoil response function without and with back-scattering correction, respectively), as well as the Sears function with a compressibility correction. We further consider the correction derived by Santana, Schram & Desmet (2016) for the back-scattering term, which is otherwise only known analytically as result of an approximation affecting mainly low frequencies. Figure 9 shows power spectral density predictions for the wind turbine test case using the revised Amiet model. Note how the first-order high-frequency response function is a relatively poor approximation of the result obtained with the Sears function, considered to be more reliable in this case; however, adding the trailing-edge back scattering, i.e. the second-order term, improves agreement with the result given by the Sears response function. This is further improved when correcting the approximate analytical solution of the back-scattering term (see (2.16)) for low-frequency effects as proposed by Santana *et al.* (2016).

4.4.3. *Time between blade chops*

In § 3.2.1, we calculated the time between blade chops as seen by the observer and discussed the differences between our derivation and the results found in Amiet (1989) and Karve *et al.* (2018). Figure 10 shows power spectral density predictions for the wind turbine case with the revised Amiet model by using the time between blade chops as
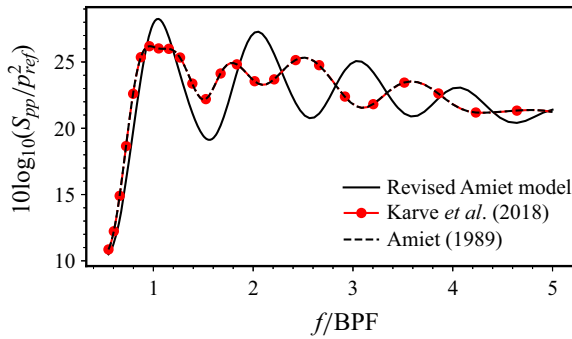
Figure 10. Far-field pressure power spectral density for wind turbine with Sears response function using different results for the time between blade chops as seen from the observer in Amiet's theory. Present formulation is found in § 3.2.1 and the other two formulations are from Amiet (1989) and Karve *et al.* (2018).

calculated in this paper and in those two references. It can be seen that the latter two sets of results overlap in this test case. Both lack the characteristic features of haystacking around multiples of the blade-passing frequency and, crucially, both disagree with the present formulation. In turn, this means that they are also in disagreement with the rotational model which follows a completely different derivation. This is evidence of the correctness of the revised Amiet model presented in this paper.

4.5. *Comparison with experimental data*

Go *et al.* (2024) conducted an experimental investigation of the noise produced by an open and a shrouded propeller interacting with grid-generated turbulence in the anechoic wind tunnel at the University of Bristol. The tests were undertaken with a two-bladed 12-in.diameter propeller at a rotational speed of 6000 RPM. The wind tunnel speed was 5 m s^{-1}. Detailed hotwire measurements were carried out at multiple locations upstream of the propeller to characterise the mean flow and incoming turbulence. The turbulence integral length scale was $\Lambda = 30.2$ mm and the mean-square fluctuating velocity was $\overline{u^2} = 0.0841$ m^2 s^{-2}. Far-field acoustic measurements were also taken when the propellers were operating with and without grid-generated turbulence. The measurement with a clean inflow allows for the separation of turbulence ingestion noise from other noise sources. For further detail on the experimental methodology the reader is referred to Go *et al.* (2024).

In this section we compare the rotational model and the revised Amiet model against the experimental data published by Go *et al.* (2024) in order to validate both models and assess their accuracy. Note that the Sears response function was used in all computations here, as the propeller blades are considered acoustically compact in the chordwise direction. All the noise data presented here are for an observer at 1.5 m from the propeller hub.

Figure 11 shows the sound pressure level (SPL) at 1 Hz bandwidth at microphone polar angles of 70°, 100° and 135° (0° corresponds to an observer upstream in the propeller axis). Experimental measurements are presented with the turbulence grid located upstream and with a clean inflow, referred to as the 'Grid' and 'Clean' cases in figure 11. The 'Clean' inflow spectra are characterised by tonal noise at the blade-passing frequency and its first harmonic, followed by broadband noise at higher frequencies. The 'Grid' spectra show additional tonal peaks that become progressively broader with increasing frequency up to the tenth harmonic of the blade-passage frequency. This feature is more clearly visible at the polar angle of 135° and is characteristic of haystacking associated with turbulence ingestion noise. The predictions of the revised Amiet model and of the
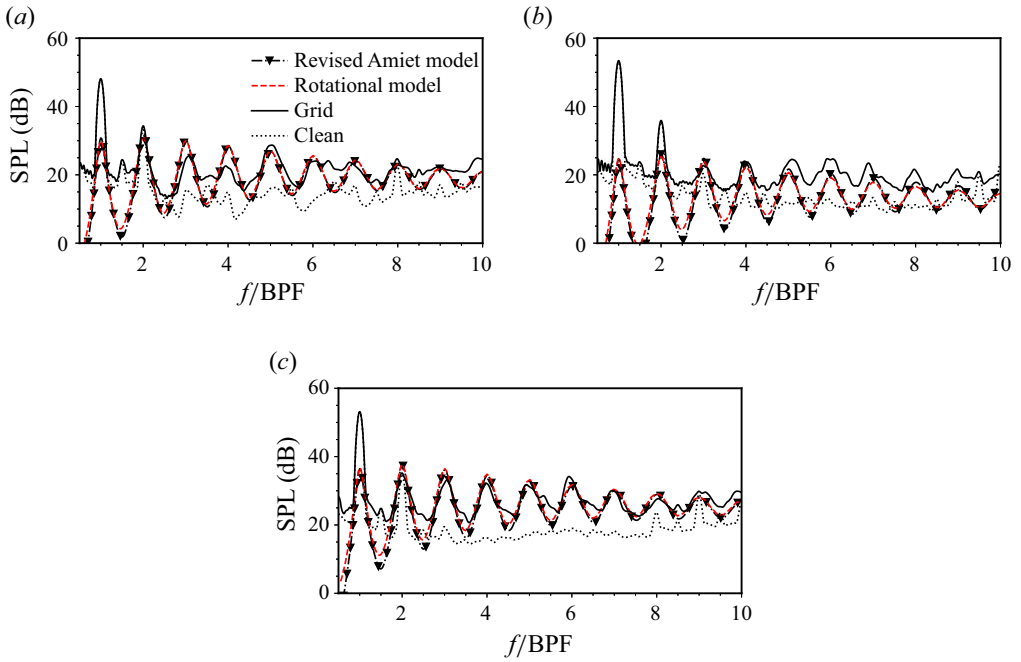
Figure 11. SPL at 1 Hz bandwidth at microphone polar angles (*a*) 70°, (*b*) 100° and (*c*) 135°. 'Grid' refers to experimental results with the turbulence grid installed. 'Clean' refers to experimental results without the turbulence grid installed.
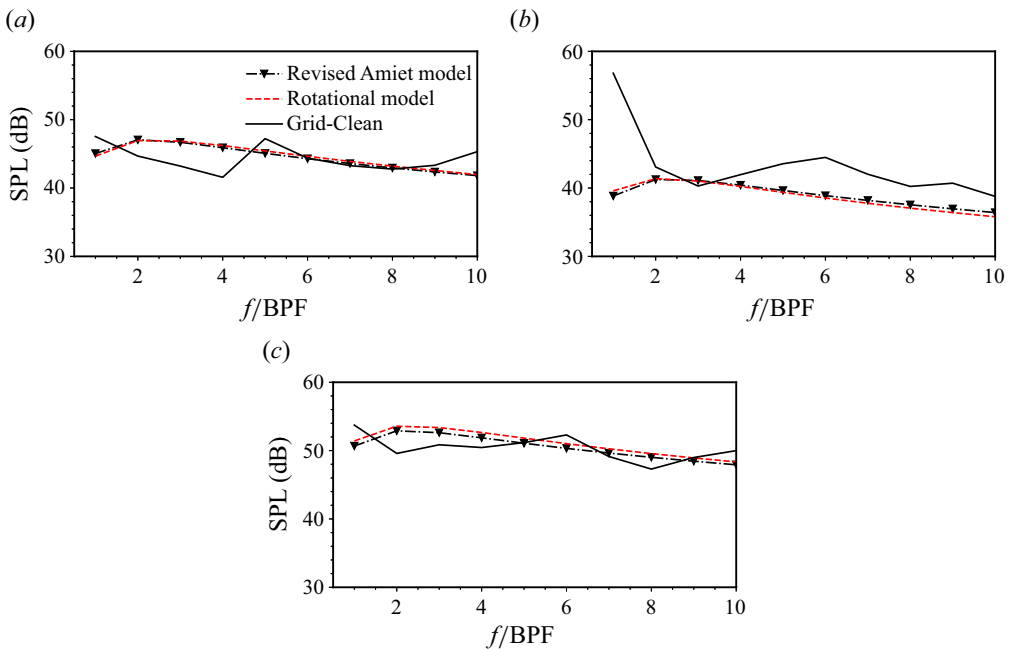

Figure 12. SPL at 200 Hz bandwidth at microphone polar angles (*a*) 70°, (*b*) 100° and (*c*) 135°. 'Grid-Clean' refers to clean inflow measurements subtracted from measurements with the turbulence grid installed.
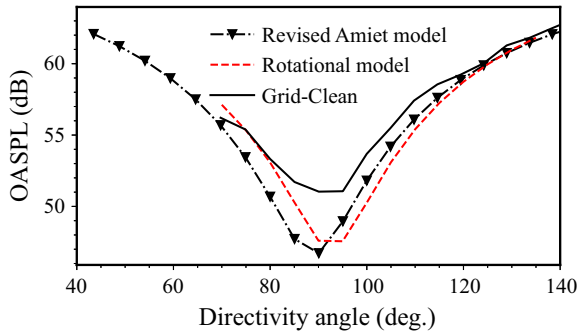
Figure 13. Overall SPL directivity (excluding energy between 0 and 300 Hz to avoid the first blade-passage frequency).

rotational model are almost indistinguishable. The two models are in good agreement with the measured spectra. Noise is under-predicted at the blade-passage frequency and its first harmonic, as the measured spectra include loading and thickness noise. For higher frequencies, agreement is particularly good between the measured and predicted tonal peaks for observers at polar angles of $70°$ and $135°$. The predicted troughs are generally lower than the measured troughs which could be explained by the presence of other noise sources captured by the measurements (Go *et al.* 2024).

Figure 12 shows the SPL at 200 Hz bandwidth which corresponds to the blade-passage frequency. The model predictions are compared to the difference between the measured spectra with and without the turbulence grid installed ('Grid-Clean'). This subtraction separates turbulence ingestion noise from other noise sources. Excellent agreement is observed at polar angles of $70°$ and $135°$, with differences under 3 dB.

The measured overall SPL directivity is compared to model predictions in figure 13. The acoustic energy associated with the blade-passing frequency tone was excluded from the calculation of the overall SPL to avoid contamination from loading and thickness noise. As can be seen, the revised Amiet model and the rotational model are in close agreement, while they underpredict noise levels by as much as 5 dB at microphone locations near the plane of the propeller. However, the models are in good quantitative agreement with experiment for polar angles under $80°$ and above $95°$.

5. Conclusions

Amiet's theory has been widely used in the study of leading-edge and trailing-edge noise of stationary aerofoils (Amiet 1975, 1976*b*; Moreau & Roger 2005; Zhong *et al.* 2020). The extension of those models to rotating blades (Schlinker & Amiet 1981) has also been widely adopted in the study of trailing-edge noise (Paterson & Amiet 1979; Rozenberg, Roger & Moreau 2010; Casalino *et al.* 2021) and turbulence ingestion noise (Karve *et al.* 2018; Halimi, Marinus & Larbi 2019). The semi-analytical model of Amiet is often preferred to other approaches mainly because it is formulated in the frequency domain, enabling statistical descriptions of turbulence, and it has a low computational cost. However, its elegance and simplicity are owed to a number of assumptions about the blade geometry, the incident turbulent flow field and the temporal–spatial scales of blade geometry, motion and noise sources.

Hanson (1974) observed that turbulent eddies are stretched on approach to a rotor and chopped several times. The partial blade-to-blade correlation leads to narrow-band noise

around harmonics of the blade-passing frequency, also known as haystacking. In this paper, we have shown that previous derivations of Amiet's theory did not agree on a key calculation in order to account for blade-to-blade correlation of the noise sources (Paterson & Amiet 1979; Amiet 1989; Karve *et al.* 2018). A corrected derivation of the time between blade chops of the same turbulent eddy as heard by the observer was presented.

Concurrently, we have developed a turbulence ingestion noise model for rotating blades using a similar theoretical basis as Sinayoko *et al.* (2013). Crucially, this model takes into account noise source correlation across the span and between blades in an exact manner. Both this new model and Amiet's theory were applied to the study of homogeneous isotropic turbulence ingestion by a model cooling fan, wind turbine and aircraft propeller. Comparisons between the two models confirmed that the revised formulation of Amiet's theory leads to accurate predictions of haystacking tones, a key feature of far-field noise spectra due to turbulence ingestion noise. This observation was validated through comparisons with the experimental data of Go *et al.* (2024), where good agreement was generally found.

Amiet's theory is typically used in conjunction with strip theory. The total far-field noise is calculated as the sum of the individual, uncorrelated contributions of each strip. In addition, an infinite-span assumption must be made in order to achieve convergence with the number of strips. Conversely, the noise model developed in this paper accounts for correlation across the span and for finite-span effects. Comparisons between the two models thus enabled us to verify that Amiet's theory remains accurate in spite of the oftentimes ill-justified assumptions, particularly in the low-frequency regime. Agreement was particularly exceptional in the model propeller and wind turbine. In what concerns the model cooling fan, it was shown that large ratios between the turbulence length scale and the blade span deteriorate the quality of predictions, but even in that case generally good agreement is observed.

In this paper, we also investigated an approximate formulation of the full rotational model in the low blade pitch angle limit. The benefits of such formulation are twofold: (i) substantial speed-ups in calculations are achieved through simplification of the analytic model; and (ii) experimental or numerical input to this theory would be reduced to the streamwise component of the turbulent velocity on approach to the rotor. Ultimately, it was shown that for rotating blades operating at low angles of attack and low advance ratio, very accurate predictions can be achieved with the simplified model. In the model rotors studied in this paper, these conditions were met for the aircraft propeller and the wind turbine.

Overall, this paper has shown that Amiet's theory can, in practice, be used to accurately predict turbulence ingestion noise from open rotors. This is particularly important in applications where fast predictions are required because other frequency-domain models such as those of Majumdar & Peake (1998) and Glegg *et al.* (2012), or even time-domain methods such as that of Glegg *et al.* (2015), are expensive to evaluate.

Declaration of interests. The authors report no conflict of interest.

Author ORCIDs.

Henrique Raposo https://orcid.org/0000-0002-7573-2789.

Appendix A

The turbulent upwash velocity cross-spectrum is calculated using the Jacobi–Anger expansion introduced in (2.29) for the mth and kth blades, and (2.30) in (2.28). The resulting expression for the full cross-spectrum of the blade-normal gust velocity component is given by

$$
S_{ww}^{(m,k)}(r, r', \omega) = \frac{1}{U_z} \int_0^{+\infty} \int_0^{2\pi} k_R \times \sum_{p=-\infty}^{+\infty} \exp(\mathrm{i}p(\phi_m - \phi_k))
$$

$$
\times \Bigg[\Phi_{11}(k_z, k_R, k_\gamma) \Big[N_{p+1,1}^{(m)} \left(N_{p-1,1}^{(k)} - N_{p+1,1}^{(k)} \right)
$$

$$
+ N_{p-1,1}^{(m)} \left(N_{p+1,1}^{(k)} - N_{p-1,1}^{(k)} \right) \Big]
$$

$$
+ \Phi_{12}(k_z, k_R, k_\gamma) \Big[N_{p-1,1}^{(m)} \left(N_{p+1,2}^{(k)} + N_{p-1,2}^{(k)} \right)
$$

$$
- N_{p+1,1}^{(m)} \left(N_{p-1,2}^{(k)} + N_{p+1,2}^{(k)} \right) \Big]
$$

$$
+ \Phi_{13}(k_z, k_R, k_\gamma) \Big[N_{p-1,1}^{(m)} N_{p,3}^{(k)} - N_{p+1,1}^{(m)} N_{p,3}^{(k)} \Big]
$$

$$
+ \Phi_{21}(k_z, k_R, k_\gamma) \Big[N_{p-1,2}^{(m)} \left(N_{p+1,1}^{(k)} - N_{p-1,1}^{(k)} \right)
$$

$$
+ N_{p+1,2}^{(m)} \left(-N_{p-1,1}^{(k)} + N_{p+1,1}^{(k)} \right) \Big]
$$

$$
+ \Phi_{22}(k_z, k_R, k_\gamma) \Big[N_{p-1,2}^{(m)} \left(N_{p+1,2}^{(k)} + N_{p-1,2}^{(k)} \right)
$$

$$
+ N_{p+1,2}^{(m)} \left(N_{p-1,2}^{(k)} + N_{p+1,2}^{(k)} \right) \Big]
$$

$$
+ \Phi_{23}(k_z, k_R, k_\gamma) \Big[N_{p-1,2}^{(m)} N_{p,3}^{(k)} + N_{p+1,2}^{(m)} N_{p,3}^{(k)} \Big]
$$

$$
+ \Phi_{31}(k_z, k_R, k_\gamma) N_{p,3}^{(m)} \left(N_{p+1,1}^{(k)} - N_{p-1,1}^{(k)} \right)
$$

$$
+ \Phi_{32}(k_z, k_R, k_\gamma) N_{p,3}^{(m)} \left(N_{p+1,2}^{(k)} + N_{p-1,2}^{(k)} \right)
$$

$$
+ \Phi_{33}(k_z, k_R, k_\gamma) N_{p,3}^{(m)} N_{p,3}^{(k)} \Bigg] \mathrm{d}k_R \, \mathrm{d}k_\gamma, \tag{A1}
$$

where

$$
\left.
\begin{aligned}
N_{p,1}^{(m)} &= \frac{\mathrm{i}\sin\alpha}{2}(i)^p \mathrm{J}_p(k_R r)\mathrm{e}^{-\mathrm{i}pk_\gamma}, \\
N_{q,1}^{(k)} &= \frac{\mathrm{i}\sin\alpha'}{2}(-i)^q \mathrm{J}_q(k_R r')\mathrm{e}^{\mathrm{i}qk_\gamma}, \\
N_{p,2}^{(m)} &= \frac{\sin\alpha}{2}(i)^p \mathrm{J}_p(k_R r)\mathrm{e}^{-\mathrm{i}pk_\gamma}, \\
N_{q,2}^{(k)} &= \frac{\sin\alpha'}{2}(-i)^q \mathrm{J}_q(k_R r')\mathrm{e}^{\mathrm{i}qk_\gamma}, \\
N_{p,3}^{(m)} &= -\cos\alpha\,(i)^p \mathrm{J}_p(k_R r)\mathrm{e}^{-\mathrm{i}pk_\gamma}, \\
N_{q,3}^{(k)} &= -\cos\alpha'\,(-i)^q \mathrm{J}_q(k_R r')\mathrm{e}^{\mathrm{i}qk_\gamma},
\end{aligned}
\right\}
\tag{A2}
$$

and $k_z = (\omega - p\Omega)/U_\infty$.

REFERENCES

AMIET, R.K. 1974 Compressibility effects in unsteady thin-airfoil theory. *AIAA J.* **12** (2), 252–255.

AMIET, R.K. 1975 Acoustic radiation from an airfoil in a turbulent stream. *J. Sound Vib.* **41** (4), 407–420.

AMIET, R.K. 1976*a* High frequency thin-airfoil theory for subsonic flow. *AIAA J.* **14** (8), 1076–1082.

AMIET, R.K. 1976*b* Noise due to turbulent flow past a trailing edge. *J. Sound Vib.* **47** (3), 387–393.

AMIET, R.K. 1977 Noise produced by turbulent flow into a propeller or helicopter rotor. *AIAA J.* **15** (3), 307–308.

AMIET, R.K. 1989 Noise produced by turbulent flow into a rotor: theory manual for noise calculation. *Tech. Rep.* NASA-CR-181788. NASA.

AMIET, R.K. 1993 On the second-order solution to the Sears problem for compressible flow. *J. Fluid Mech.* **254**, 213–228.

BLANDEAU, V.P. & JOSEPH, P.F. 2011 Validity of Amiet's model for propeller trailing-edge noise. *AIAA J.* **49** (5), 1057–1066.

BROUCKAERT, J.F., MIRVILLE, F., PHUAH, K. & TAFERNER, P. 2018 Clean sky research and demonstration programmes for next-generation aircraft engines. *Aeronaut. J.* **122** (1254), 1163–1175.

CASALINO, D., GRANDE, E., ROMANI, G., RAGNI, D. & AVALLONE, F. 2021 Definition of a benchmark for low Reynolds number propeller aeroacoustics. *Aerosp. Sci. Technol.* **113**, 106707.

CASPER, J. & FARASSAT, F. 2004 Broadband trailing edge noise predictions in the time domain. *J. Sound Vib.* **271** (1), 159–176.

CHRISTOPHE, J. 2011 Application of hybrid methods to high frequency aeroacoustics. PhD thesis, Université Libre de Bruxelles.

CHRISTOPHE, J., ANTHOINE, J. & MOREAU, S. 2009 Amiet's theory in spanwise-varying flow conditions. *AIAA J.* **47** (3), 788–790.

GARRICK, I.E. & WATKINS, C.E. 1953 A theoretical study of the effect of forward speed on the free-space sound-pressure field around propellers. *Tech. Rep.* NACA-TN-3018. NACA.

GLEGG, S. & DEVENPORT, W. 2017 *Aeroacoustics of Low Mach Number Flows: Fundamentals, Analysis, and Measurement*. Academic, Elsevier.

GLEGG, S., MORTON, M. & DEVENPORT, W. 2012 Rotor inflow noise caused by a boundary layer: theory and examples. *18th AIAA/CEAS Aeroacoustics Conference*. AIAA Paper 2012-2263.

GLEGG, S.A., DEVENPORT, W. & ALEXANDER, N. 2015 Broadband rotor noise predictions using a time domain approach. *J. Sound Vib.* **335**, 115–124.

GO, S.T., KINGAN, M.J., BOWEN, L. & AZARPEYVAND, M. 2024 Noise of a shrouded propeller due to ingestion of grid-generated turbulence. *J. Sound Vib.* **571**, 118044.

GRAHAM, J.M.R. 2017 Rapid distortion of turbulence into an open turbine rotor. *J. Fluid Mech.* **825**, 764.

HALIMI, A., MARINUS, B.G. & LARBI, S. 2019 Analytical prediction of broadband noise from mini-RPA propellers with serrated edges. *Intl J. Aeroacoust.* **18** (4–5), 517–535.

HANSON, D.B. 1974 Spectrum of rotor noise caused by atmospheric turbulence. *J. Acoust. Soc. Am.* **56** (1), 110–126.

HOMICZ, G.F. & GEORGE, A.R. 1974 Broadband and discrete frequency radiation from subsonic rotors. *J. Sound Vib.* **36** (2), 151–177.

HUBBARD, H.H. 1991 *Aeroacoustics of Flight Vehicles: Theory and Practice*. NASA Office of Management, Scientific and Technical Information Program.

KARVE, R., ANGLAND, D. & NODÉ-LANGLOIS, T. 2018 An analytical model for predicting rotor broadband noise due to turbulent boundary layer ingestion. *J. Sound Vib.* **436**, 62–80.

LOWSON, M.V. & OLLERHEAD, J.B. 1969 A theoretical study of helicopter rotor noise. *J. Sound Vib.* **9** (2), 197–222.

MAJUMDAR, S.J. & PEAKE, N. 1998 Noise generation by the interaction between ingested turbulence and a rotating fan. *J. Fluid Mech.* **359**, 181–216.

MOREAU, S. & ROGER, M. 2005 Effect of angle of attack and airfoil shape on turbulence-interaction noise. *11th AIAA/CEAS Aeroacoustics Conference*. AIAA Paper 2005-2973.

MORFEY, C.L. & TANNA, H.K. 1971 Sound radiation from a point force in circular motion. *J. Sound Vib.* **15** (3), 325–351.

PATERSON, R.W. & AMIET, R.K. 1979 Noise of a model helicopter rotor due to ingestion of turbulence. *Tech. Rep.* NASA-CR-3213. NASA.

POSSON, H., MOREAU, S. & ROGER, M. 2010 On the use of a uniformly valid analytical cascade response function for fan broadband noise predictions. *J. Sound Vib.* **329** (18), 3721–3743.

ROBISON, R.A.V. & PEAKE, N. 2014 Noise generation by turbulence–propeller interaction in asymmetric flow. *J. Fluid Mech.* **758**, 121–149.

ROZENBERG, Y., ROGER, M. & MOREAU, S. 2010 Rotating blade trailing-edge noise: experimental validation of analytical model. *AIAA J.* **48** (5), 951–962.

SANTANA, L.D., SCHRAM, C. & DESMET, W. 2016 Low-frequency extension of Amiet's theory for compact airfoil noise predictions. *J. Sound Vib.* **372**, 342–356.

SCHLINKER, R.H. & AMIET, R.K. 1981 Helicopter rotor trailing edge noise. *Tech. Rep.* NASA-CR-3470. NASA.

SEVIK, M. 1974 Sound radiation from a subsonic rotor subjected to turbulence. *Fluid Mech. Acoust. Des. Turbomach.* **Pt. 2**, 493–512.

SHARLAND, I.J. 1964 Sources of noise in axial flow fans. *J. Sound Vib.* **1** (3), 302–322.

SIMONICH, J.C., AMIET, R.K., SCHLINKER, R.H. & GREITZER, E.M. 1986 Helicopter rotor noise due to ingestion of atmospheric turbulence. *Tech. Rep.* NASA-CR-3973. NASA.

SINAYOKO, S., KINGAN, M. & AGARWAL, A. 2013 Trailing edge noise theory for rotating blades in uniform flow. *Proc. R. Soc. Lond.* A **469** (2157), 20130065.

SMITH, S.N. 1972 Discrete frequency sound generation in axial flow turbomachines. *Tech. Rep.* 3079. Ministry of Defence, Aeronautical Research Council.

WILSON, D.K. 1997 Three-dimensional correlation and spectral functions for turbulent velocities in homogeneous and surface-blocked boundary layers. *Tech. Rep.* ARL-TR-1287. Army Research Laboratory.

ZHONG, S., ZHANG, X., PENG, B. & HUANG, X. 2020 An analytical correction to Amiet's solution of airfoil leading-edge noise in non-uniform mean flows. *J. Fluid Mech.* **882**, A29.